

## THE LOW-MASS IMF IN THE 30 DORADUS STARBURST CLUSTER

M. ANDERSEN

Space Science Department, European Space Agency, Keplerlaan 1, 2200 AG Noordwijk, Netherlands

H. ZINNECKER

Astrophysical Institute Potsdam, An der Sternwarte 16, 14482 Potsdam Germany

A. MONETI

Institut d'Astrophysique, Paris 98bis Blvd Arago, F-75014 Paris, France

M. J. MCCAUGHREAN

Space Science Department, European Space Agency, Keplerlaan 1, 2200 AG

B. BRANDL

Leiden Observatory, P.O. Box 9513, 2300 RA Leiden, Netherlands

W. BRANDNER

Max-Planck-Institut für Astronomie, Königstuhl 17, 69117 Heidelberg, Germany

G. MEYLAN

Laboratoire d'Astrophysique, Ecole Polytechnique Fédérale de Lausanne (EPFL), Observatoire, CH - 1290 Sauverny, Switzerland

AND

D. HUNTER

Lowell Observatory, 1400 West Mars Hill Road, Flagstaff, AZ 86001

*Draft version September 27, 2018*

### ABSTRACT

We present deep Hubble Space Telescope (HST) NICMOS 2 *F160W* band observations of the central  $56'' \times 57''$  ( $14\text{pc} \times 14.25\text{pc}$ ) region around R136 in the starburst cluster 30 Dor (NGC 2070) located in the Large Magellanic Cloud. Our aim is to derive the stellar Initial Mass Function (IMF) down to  $\sim 1 M_{\odot}$  in order to test whether the IMF in a massive metal-poor cluster is similar to that observed in nearby young clusters and the field in our Galaxy. We estimate the mean age of the cluster to be 3 Myr by combining our *F160W* photometry with previously obtained HST WFPC2 optical *F555W* and *F814W* band photometry and comparing the stellar locus in the color-magnitude diagram with main sequence and pre-main sequence isochrones. The color-magnitude diagrams show the presence of differential extinction and possibly an age spread of a few Myr. We convert the magnitudes into masses adopting both a single mean age of 3 Myr isochrone and a constant star formation history from 2 to 4 Myr. We derive the IMF after correcting for incompleteness due to crowding. The faintest stars detected have a mass of  $0.5 M_{\odot}$  and the data are more than 50% complete outside a radius of 5 pc down to a mass limit of  $1.1 M_{\odot}$  for 3 Myr old objects. We find an IMF of  $\frac{dN}{d\log M} \propto M^{-1.20 \pm 0.2}$  over the mass range  $1.1\text{--}20 M_{\odot}$  only slightly shallower than a Salpeter IMF. In particular, we find no strong evidence for a flattening of the IMF down to  $1.1 M_{\odot}$  at a distance of 5 pc from the center, in contrast to a flattening at  $2 M_{\odot}$  at a radius of 2 pc, reported in a previous optical HST study. flattening at  $2 M_{\odot}$  at a radius of 2 pc previously found. We examine several possible reasons for the different results including the possible presence of mass segregation and the effects of differential extinction, particularly for the pre-main sequence sources. If the IMF determined here applies to the whole cluster, the cluster would be massive enough to remain bound and evolve into a relatively low-mass globular cluster.

*Subject headings:* stars: mass function — stars: pre-main sequence — stars: formation — globular clusters and associations: individual(30 Dor)

### 1. INTRODUCTION

The shape of the stellar Initial Mass Function (IMF) and whether it is universal or not are key issues in astrophysics. For clusters within 2 kpc, there is no compelling evidence for variations in the stellar IMF (e.g.

Meyer et al. 2000; Kroupa 2002; Chabrier 2005) or the brown dwarf IMF (e.g. Andersen et al. 2008). However, these clusters only span a limited range in total cluster mass ( $10^2 - 10^3 M_{\odot}$ ) and all have a metallicity similar to the solar value. Thus, we are forced to observe more extreme regions of star formation in search of variations in the IMF as a function of environment. It has been suggested that the shape of the IMF and in particular the characteristic mass where the IMF flattens from a Salpeter power-law could depend on the metallicity in the molecular cloud out of which the stars are formed. Low & Lynden-Bell (1976), Larson (1998), and Omukai (2000) suggest that a lower metallicity results in higher temperatures in the molecular cloud which would increase the Jeans mass. This would in turn result in a top heavy IMF relative to the solar metallicity IMF.

The closest place with massive metal-poor young star clusters is the Large Magellanic Cloud (LMC). The metallicity is only  $\frac{1}{3} - \frac{1}{2}$  the solar value (Smith 1999) and star clusters can be studied in some detail despite a distance of  $\sim 50$  kpc (Westerlund 1997). Of particular interest is the 30 Dor cluster which is powering the most luminous HII region in the Local Group (Kennicutt 1984). The cluster has a mass of at least  $2.2 \times 10^4 M_{\odot}$  within a radius of 4.7 pc (Hunter et al. 1995) and is a relatively low-mass analog to the more distant starburst clusters. R136 lies at the center of the 30 Dor cluster and has long commanded significant attention: Once thought to be a single  $\sim 1000 M_{\odot}$  star (Cassinelli et al. 1981), the region is now known to host numerous O stars (Melnick 1985; Weigelt & Baier 1985; Pehlemann et al. 1992; Campbell et al. 1992).

The whole 30 Dor region, with a size of 200 pc, appears to have an age spread of  $\sim 20$  Myr (McGregor & Hyland 1981; Selman et al. 1999) with stars still forming (Rubio et al. 1992; Maercker & Burton 2005). R136 appears to have a much smaller age spread of at most a few Myr (Melnick 1985; Brandl et al. 1996; Massey & Hunter 1998). An age of 2 Myr or less is inferred from spectroscopy of the O stars in the very cluster center (Massey & Hunter 1998), whereas the intermediate mass population is thought to be  $\sim 3-4$  Myr old (Hunter et al. 1995).

Massey & Hunter (1998) obtained HST spectroscopy of the 65 bluest and most luminous sources within  $17''$  of the cluster center. They derived the IMF over the mass range  $15-120 M_{\odot}$  and found it to be well approximated by a power-law  $\frac{dN}{d \log M} \propto M^{\Gamma}$  with a slope of  $\Gamma = -1.3 \pm 0.1$ , consistent with a Salpeter slope IMF (Salpeter 1955). Hunter et al. (1995, 1996) obtained *F555W* (*V*) and *F814W* (*i*) band optical photometry utilizing HST/WFPC2 in order to resolve the cluster's intermediate mass stellar population. The IMF derived for different annuli out to a radius of 4.7 pc was found to be in the range  $-1.46 < \Gamma < -1.17$  for the mass range  $2.8-15 M_{\odot}$ , again consistent with a Salpeter slope IMF. Massey & Hunter (1998) combined their results for the high-mass IMF with the results from Hunter et al. (1995, 1996) in order to constrain the IMF from  $2.8 M_{\odot}$  up to  $120 M_{\odot}$ . Comparing the number of high-mass stars predicted by the intermediate-mass IMF from Hunter et al. (1996), they found the number of massive stars was consistent with a single power-law IMF with a Salpeter

slope, i.e.  $\Gamma = -1.35$ .

Combining the two data sets used in Hunter et al. (1995, 1996), Sirianni et al. (2000) derived the IMF between  $1.35 M_{\odot}$  and  $6.5 M_{\odot}$ , extending the IMF determination into the mass range where the stars are still in their pre-main sequence phase. The IMF was derived in a box with the dimensions  $\sim 30''.4 \times 26''.8''$  ( $7.6 \text{ pc} \times 6.7 \text{ pc}$ ), but excluding the inner most  $13''.6 \times 8.6''$  ( $3.5 \text{ pc} \times 2.2 \text{ pc}$ ). Again, a Salpeter slope was found down to  $2 M_{\odot}$ , but the IMF was found to be flatter than Salpeter,  $\Gamma = -0.27 \pm 0.08$ , between  $1.35 M_{\odot}$  and  $2 M_{\odot}$ , suggesting the characteristic mass is higher in this massive, metal-poor cluster than  $\sim 0.5 M_{\odot}$  as found in the Galactic field (Kroupa 2002).

The foreground ( $A_V = 0.7$  mag) and differential extinction ( $A_V \sim 0 - 2$  mag) within the cluster (Brandl et al. 1996) makes it desirable to observe the cluster in the infrared, for example the *H* band where the extinction is less than 20% that of the *V* band. In addition, pre-main sequence stars are often associated with circumstellar disks and outflows which will introduce additional extinction for the clusters low-mass content.

We have observed R136 with HST/NICMOS Camera 2 through the *F160W* band, which is similar to a ground-based *H* filter. The observations were aimed at being sensitive to objects below  $1 M_{\odot}$  for a stellar population with an age of 3 Myr. Preliminary results have previously been presented in Zinnecker et al. (1999, 2002), and Andersen et al. (2005).

The paper is structured as follows. The data and their reduction is described in Section 2. Section 3 shows the results for the *F160W* band imaging. The IMF is derived in Section 4 and compared with the IMF derived by Sirianni et al. (2000). We point out several plausible reasons for the different results in the optical and near-infrared, including mass segregation, and differential extinction. Finally, our conclusions are presented in Section 5.

## 2. DATA REDUCTION AND PHOTOMETRY

### 2.1. Observations

We have obtained HST/NICMOS Camera 2 images through the *F160W* band of the central  $56'' \times 57''$  region around R136 in the 30 Dor cluster (HST program ID 7370). The observations were centered on the cluster (RA,DEC)=(05:38:43.3,-69:06:08) and on two adjacent control fields centered on (05:38:42.4,-68:52:00), and (05:38:56.9,-68:52:00). The observing dates were Oct 14 and 16, 1997. The field-of-view of the  $256 \times 256$  pixel NICMOS Camera 2 is  $19'' \times 19''$  with a pixel scale of  $0''.075$ , resulting in Nyquist sampling of diffraction-limited *F160W* band data. Each position in a  $3 \times 3$  mosaic centered on R136 was observed four times with small dithers of  $\sim 16$  pixels. The data were obtained in non-destructive MULTIACCUM mode such that the photometry of the bright stars can be retrieved due to the first short integration in each exposure. The integration time for each dither position was 896 seconds, resulting in a total integration time of 3584 seconds for each position in the mosaic. The two control fields were observed in a similar manner.

The location of the mosaic is shown in Fig. 1 and the NICMOS mosaic is shown in Fig. 2. The faintest stars

visible with the stretch used here have an *F160W* magnitude of  $\sim 21.5$  mag, corresponding to a mass of  $0.8 M_{\odot}$ , based on the pre-main sequence models of Siess et al. (2000), adopting an age of 3 Myr (Hunter et al. 1995), half solar metallicity, and an extinction of  $A_V = 1.85$  mag (see Section 3.2). For comparison, the similar detection limit in an uncrowded environment without nebulosity would be  $\sim 23.5$  mag according to the NICMOS exposure time calculator.

### 2.2. Data reduction

Each individual image was processed through the *calnica* and *calnicb* pipelines as well as the *biaseq* and *pedsky* procedures within the IRAF environment. The tasks are described in detail in the NICMOS Data Handbook. We used synthetic dark frames and flat fields created for the appropriate instrument temperature at each exposure. The *biaseq* task corrects differences in bias levels for each chip between different sub-exposures. The *pedsky* task corrects differences in the bias level for each quadrant of the chip when the array is reset before the exposure. The data for each position in the mosaic were combined using the *drizzle* task. The reduced pixel size ( $0''.0375$ ) was chosen as half the detector pixel size. Bad pixels, bad columns, and the coronagraphic hole were flagged as bad pixels before the images were combined.

### 2.3. Source detection and photometry

Source detection was done using *daofind* and photometry was performed via point spread function (PSF) photometry utilizing *allstar* within the IRAF environment. It was difficult to obtain a good PSF model from the data due to the high degree of crowding and the spatial variability of the PSF. Instead, the TINYTIM software (Hook & Krist 1997) was used to create a synthetic PSF. TINYTIM allows to create a PSF that varies as a function of the location on the array. The source detection and photometry was performed on each individual position in the mosaic due to the linearly varying Point Spread Function (PSF). A hot template star (O5V) was used for the spectral energy distribution in order to achieve the best fit for the brightest stars to limit their residuals. The TINYTIM PSF was created for five different positions on the NICMOS Camera 2 array and the PSFs were placed in an empty frame with the same number of pixels as the NICMOS Camera 2 array. Four frames were created with offsets between each PSF identical to the offsets used for the science data in order to replicate the data as closely as possible. The four PSF frames were then combined using *drizzle* together in the same manner as the science data and a linearly-varying PSF was created from the drizzled frame.

Source detection is complicated due to the diffraction features present in NICMOS data. Adoption of a low threshold for source detection led to numerous diffraction spots from bright stars being erroneously identified as fainter stars. Instead the source detection was done in the following way in order to limit false detections. We first detected the brightest stars (brighter than  $1000\sigma$ ) in each frame and used *allstar* to remove these with the synthetic PSF. A search for fainter stars (brighter than  $500\sigma$ ) was then performed in the frame with the

bright stars removed. Since the removal of the brightest stars also removed the diffraction pattern associated with them, we did not detect the diffraction spots as stars. The two star lists (the brightest stars and the fainter stars) were joined into one and these stars were removed from the original frame, again using *allstar*. Fainter stars are then found from the frame with the already detected stars removed. This process was iterated until stars at  $10\sigma$  peak pixel intensity over the background were detected and removed. The frame with the stars removed was then ring-median filtered to remove stellar residuals but to retain the large-scale nebulosity in each frame. The median-filtered image was then removed from the original frame and the star detection process was repeated in this frame but now continued to a detection threshold of  $5\sigma$ . A  $5\sigma$  instead of e.g. a  $3\sigma$  threshold was selected to limit the risks of false detections due to noise spikes. We finally made sure by visual inspection that every detection indeed was a point source and that it was not a spurious detection due to the diffraction spikes and spots from bright stars.

The main interest here is in the low-mass (faint) stellar content in R136 and one concern is the detection of residuals from the bright stars as false stellar objects. Some false sources were detected by *daofind* but are rejected during the PSF fitting routine. A few remained from the brightest stars. They typically produced at most a few false detections in the diffraction spikes that were  $\sim 6$ – $7$  mag fainter than the bright source. We removed these detections together with other false detection through the visual inspection of all sources. We have further utilized the artificial star experiments described below to examine how many detections are false due to the residuals from bright stars. We had only false positives associated with the brightest artificial stars ( $F160W < 12$  mag). For artificial stars fainter than  $F160W \sim 14$  mag, no false detections were present. The false detections for the bright stars were located at the diffraction spikes and would have been identified in the manual inspection of the source list.

We found a total of 10108 uniquely detected sources with a formal error smaller than 0.1 mag and brighter than  $F160W = 22.5$  mag in the 9 frames. Below this magnitude limit the incompleteness is substantial, as discussed below. Table 2 presents the list of detected stars.

### 2.4. Completeness corrections

The effects of crowding were examined by placing artificial stars in the individual frames using the PSF created from the synthetic TINYTIM PSF. The artificial stars followed a luminosity function with a similar slope to that of the observed stars (see Section 3) but with a surface density 10% that of the detected number of stars to avoid affecting the crowding characteristics of the real stars. We performed 100 artificial star experiments for each frame, for a total of 10 times more artificial stars than real stars. Fig. 3 shows the resulting recovery fractions as a function of the input magnitudes for several annuli around the cluster center. The difference of the size of the error bars as a function of distance from the cluster center is due to a lower number of artificial stars placed in the central parts of the cluster. This is a consequence of adding 10% artificial stars relative to observed stars in each artificial star experiment and the relative

number of stars in each annulus. The IMF is not determined in regions with this low completeness. We are mainly interested in the low-mass stellar content of the cluster, which is below the 50% completeness in the central parts. The uncertainty in the completeness corrections for the inner parts of the cluster will therefore not affect the conclusions drawn for the stellar populations further out.

The completeness is a strong function of the radial distance from the center. For the outer regions of the cluster, 50% or more of the stars brighter than  $F160W = 21.5$  mag are detected, whereas only the very brightest stars are detected in the innermost region. In an annulus at 0.6–1 pc radius from the center, we detect 50% or more of the stars brighter than  $F160W = 18.0$  mag. Adopting the PMS models of Siess et al. (2000) and the main sequence models of Marigo et al. (2008),  $F160W = 21.5$  mag corresponds to a  $0.8 M_{\odot}$ , half solar metallicity, 3 Myr old object, whereas  $F160W = 18$  mag corresponds to a  $7.5 M_{\odot}$  star, assuming an extinction of  $A_V = 1.85$  mag in both cases.

### 2.5. Photometric accuracy

We have investigated the accuracy of the derived photometry by using the stars detected in the overlap regions of several fields. Fig. 4 shows the difference in derived magnitude for stars detected in the overlap regions of the mosaic. Dots denote stars outside a 2 pc radius and plus signs denote stars between 1.25–2 pc radius, respectively.

The  $F160W$  band photometry has been compared with the ground-based  $H$  band photometry obtained using adaptive optics observations by Brandl et al. (1996). Fig. 4 shows the magnitude difference between the adaptive optics photometry and this study based on 829 stars common to both datasets. Stars were considered detected in both datasets if the spatial position coincided within 2.5 drizzled pixels, corresponding to  $0''.094$ . Some scatter is present between the two datasets, especially for the fainter stars. However, the median difference between the magnitudes derived for the two datasets is less than 6% for objects  $F160W < 18$  mag. We have in the following treated the  $F160W$  observations as a standard Cousins  $H$  band.

Conversely, there appears to be a tendency for the fainter stars to be brighter in the  $F160W$  data than in the  $H$  band data of Brandl et al. (1996). The tendency for the fainter stars to be skewed towards fainter  $H$  band magnitudes is an effect also seen in other comparisons between HST/NICMOS and AO data (e.g. Stolte et al. 2002) who suggest it is due to the extended halos present in AO observations around bright stars.

## 3. RESULTS

The immediate results from the  $F160W$  band HST photometry are presented. After discussing the luminosity function for different annuli, the luminosity profile for the cluster is derived. The  $F160W$  band data are combined with the optical HST data by Hunter et al. (1995) and the color-magnitude diagrams are presented. Utilizing the two color-magnitude diagrams we show that the spread observed for the higher mass stars is consistent with that expected due to reddening. We estimate the average age for the stellar population and discuss the possible presence of an age spread.

### 3.1. Luminosity functions

The star counts in the central 0.6 pc radius region is heavily affected by low number statistics, crowding even for the brightest stars, and relatively uncertain incompleteness corrections. We therefore focus on the sources outside 0.6 pc in this paper. Fig. 5 shows the  $F160W$  band luminosity functions for the 0.6–7 pc radius region of the 30 Dor cluster divided into several radial bins to show the difference in photometric depth due to crowding. Overplotted are the completeness-corrected LFs, where each bin has been divided by the corresponding recovery fraction from the artificial star experiments.

The completeness-corrected luminosity functions are relatively smooth and have been fitted with power-laws down to the 50% completeness limit. The derived slopes with their  $1\sigma$  uncertainties and the 50% completeness limits are presented in Table 1. Although the slope in the inner annulus is found to be more shallow, the derived slopes are consistent with each other within  $2\sigma$  with an average slope of 0.31 and the shallow slope is not significant.

The completeness-corrected combined histogram for the stars detected in the two off-cluster control fields is shown in the lower right panel in Fig. 5. From the histogram, it can be seen that the field star contamination found from the star counts is  $\approx 10$ –15% for the faintest stars in the 5–7 pc annulus and less closer to the center as well as for brighter stars. Although the contamination of field stars is found to be relatively small it is not negligible and they are therefore statistically subtracted from the cluster population in the following analysis (Section 4).

### 3.2. The optical-near infrared color-magnitude diagrams

Next, the  $F160W$  band photometry is combined with the optical data presented by Hunter et al. (1995). A star was considered detected in both surveys if the spatial position agreed within 2.5 drizzled NICMOS Camera 2 pixels ( $0''.094$ ). In the cases where two optical stars were located within the search radius of the star detected in the NICMOS Camera 2 observations, the brightest star was chosen as the match.

We find in total 2680 in common with the Hunter et al. (1995) survey that detected 3623 stars the inner  $35''$  of the cluster. 1848 of those sources have a combined formal photometric error in the  $F555W$ – $F160W$  color of less than 0.1 mag. Within the area covered by Hunter et al. (1995) we detect a total of 5095 sources. Most of the stars detected by the NICMOS survey but not the WFPC2 observations are fainter than  $F160W = 20$  mag. Assuming an object age of 3 Myr and an average extinction of  $A_V = 1.85$  mag (see below), the similar object would have a magnitude in the  $F814W$  band of  $\sim 22$  mag. For objects with more extinction, they will be even harder to detect in the  $F814W$  band. Hunter et al. (1995) essentially don't detect any stars within a 1 pc radius at this magnitude or fainter. Only 1 in 4 stars in the magnitude interval  $F814W = 21$ –22 mag was detected outside 1 pc. It is thus not surprising that a significant population of faint stars are detected in the NICMOS survey relative to the WFPC2 survey. Nevertheless, the lower spatial resolution of the NICMOS observations results in a low

recovery fraction at these magnitudes in the central few pc of the cluster.

The majority of the sources not detected in the NICMOS survey but at optical wavelengths are located within a radius of 1 pc. The lack of detection is due to the lower spatial resolution in this study relative to the optical HST data. The resolution is almost a factor of two better in the  $F814W$  band than in the  $F160W$  band. Sources not detected in the NICMOS data outside 1 pc are mainly due to crowding as well. Indeed, visual inspection of the location of the stars detected in the optical but not near-infrared shows they are often located either very close to the core or on the first Airy ring of a bright source.

The  $F555W$ - $F160W$  versus  $F160W$  color-magnitude diagram is shown in Fig. 6. Overplotted are a 3 Myr isochrone for the high-mass stars adopted from the Marigo et al. (2008) models and 2, 3, and 4 Myr isochrones adopted from Siess et al. (2000) for stars below  $7 M_{\odot}$ . The stars above  $7 M_{\odot}$  and up to the maximum mass we fit the IMF in Section 4.1 ( $20 M_{\odot}$ ) are all expected to be on the main sequence. Both isochrones were calculated adopting a metallicity of half the solar value, typical for the LMC (Smith 1999). The two isochrones have a small offset in both the  $V$  (0.06 mag) and  $H$  (0.07 mag) band. We have forced the Marigo et al. (2008) isochrone to match the Siess et al. (2000) isochrone at  $7 M_{\odot}$ .

It is evident there is a significant scatter in the color-magnitude diagram. The scatter is likely due to a combination of binary systems (both physical and chance alignments), differential extinction, photometric errors and a possible age spread. The median extinction is found for the main sequence part of the isochrone. For objects in the range  $7$ – $20 M_{\odot}$ , we find a median extinction of  $A_V = 1.85$  mag which is slightly higher than the reddening found by Selman et al. (1999) in the inner part of the 30 Dor region.

At masses below  $7 M_{\odot}$ , the spread in the color-magnitude diagram is larger but almost exclusively extends to the red part of the diagram. This indicates the lower-mass objects on average have an excess amount of extinction relative to the higher mass objects. Selman et al. (1999) observed stars more massive than  $10 M_{\odot}$  and would not detect the additional reddening for the lower-mass sources. The possible sources for the additional reddening is described in Sec. 3.3.

We have estimated an average age for the cluster by utilising the fact the isochrone is almost horizontal in the color range  $F555W$ - $F160W$ =1.5-2.5 mag and around  $F160W$ ~19 mag. The median  $F160W$  magnitude is 19.0 mag in this region of the color-magnitude diagram. Adopting an average extinction of  $A_V = 1.85$  mag, this corresponds to the  $F160W$  magnitudes of the 3 Myr isochrone in the same color range. We have thus adopted 3 Myr as the mean age of the low mass cluster population and a 3 Myr isochrone is adopted to create a mass-luminosity relation in order to turn the luminosities into masses for objects below  $7 M_{\odot}$  and the 3 Myr Marigo et al. (2008) isochrone above. We will in Sect. 4 the effects on the derived IMF adopting an age spread of 2 Myr.

The right hand panel in Fig. 6 shows the  $I$ - $F160W$  versus  $F160W$  color-magnitude diagram. It is evident

that the clustering around the isochrone is tighter than for the  $V$ - $F160W$  versus  $F160W$  color magnitude diagram. This is expected if a large part of the scatter is due to differential extinction. We can calculate the scatter around the main sequence in both color-magnitude diagrams and compare with the difference predicted from extinction.

If the spread in the color-magnitude diagrams is due to extinction we expect the ratio of spread in the  $V$ - $F160W$  versus  $F160W$  diagram to be ratio of the extinction in each color, i.e.  $(1 - 0.192)/(0.62 - 0.192) = 1.88$  times larger than in the  $I$ - $F160W$  versus  $F160W$  color-magnitude diagram. Since the isochrone is almost vertical in both diagrams, we have calculated the standard deviation around the reddened isochrone in both color-magnitude diagrams. We have used the stars with good photometry, better than 5% in each filter, and in the magnitude range  $13 < F160W < 17$  mag. The standard deviation found for the  $V$ - $F160W$  and  $I$ - $F160W$  color-magnitude diagrams are 0.60 mag, and 0.36 mag and the ratio is 1.7. If the measurement errors are taken into account this ratio increases. The typical errors for the culled sample are 0.04, 0.02, and 0.03 mag for the  $V$ ,  $I$ , and  $F160W$  bands, respectively. After taking the measurement errors into account, the ratio is found to be 1.9, assuming the measurement errors in two filters are independent. Due to blending, this is not necessarily the case. Thus, 1.9 is an upper limit and we thus find the ratio to be between 1.7 and 1.9, in agreement with the scatter being due to differential extinction.

Since the amount of differential extinction does not affect the  $F160W$  band photometry significantly, the single band photometry presented here is competitive with the 2-band optical photometry. There is a unique translation from the  $F160W$  band magnitude to the object mass for the majority of the mass range. For the optical photometry, the color information is used to determine the extinction and the mass function is thus effectively determined by the de-reddened  $V$  band magnitude.

### 3.3. The differences between the optical and near-infrared HST observations

The main advantage of the optical relative to the near-infrared HST photometry is the improved resolution due to the smaller diffraction limit. The stellar content can therefore be resolved to lower masses closer to the cluster core than is possible with the near-infrared observations. However, phenomena associated with the star formation process can introduce additional reddening that can complicate the derivation of the low-mass IMF from optical data. The low-mass objects may still be associated with a circumstellar disk. There is evidence from e.g. the Orion Nebula Cluster that circumstellar disks can survive the UV radiation from massive stars (Robberto et al. 2004). Even if the disks are being evaporated by the radiation field from the early type stars, the evaporated material will be a further source of reddening. Patchy extinction associated with the 30 Dor complex and located in the foreground of R 136 will be an additional source of differential reddening. There are signs in the optical images presented in Fig. 1 of Sirianni et al. (2000) of patches of extinction, e.g. to the east-north-east of the cluster center. If variable extinction is present or if a significant fraction of the stars are associated with

disks or outflows, an extinction limited sample has to be created in order to avoid a biases against detection of the low-mass stars.

The near-infrared photometry is effected by differential extinction as well but the effect is less than 20% of that measured in the  $V$  band. Thus, whereas the IMF derived from optical observations where an extinction limited sample is not defined might be severely affected for the low-mass objects, the effect on near-infrared observations is modest. Therefore, in the outer parts of the cluster where crowding is a smaller issue than closer to the center, the near-infrared observations are more suitable to detect and characterise the low-mass stellar population in the cluster.

On the other hand, single band photometry has the disadvantage that there is no information on the age of individual objects. We investigate in the next Section how this might affect the derived IMF. We note that if differential extinction is present, the situation is no better for the optical photometry. Even though the cluster was observed through two filters in the optical, there is still a degeneracy between age and extinction. Sirianni et al. (2000) converted the  $V-i$  photometry into an effective temperature and used that effective temperature to obtain a bolometric correction. Without de-reddening the sources, the age of a cluster member can be in error and hence the mass estimates will be uncertain.

#### 4. ANALYSIS

We construct a mass-luminosity relation by combining the main sequence models by Marigo et al. (2008), and the pre-main sequence models of Siess et al. (2000) in order to infer the stellar mass from the  $F160W$  band magnitude. We then derive the mass functions for R136 outside 0.6 pc where the 50% completeness limit corresponds to a stellar mass below  $10 M_{\odot}$ . Deriving the IMF this way is a well established procedure (Lada & Lada 2003; Muench et al. 2002). We further discuss the potential effect of extinction on the derived IMF. Finally, we search for evidence for mass segregation in the outer parts of the cluster using the cumulative luminosity functions.

##### 4.1. Deriving the mass function

A mass-luminosity relation is needed to convert the derived  $F160W$  band magnitude for each star to a mass. We use the Siess et al. (2000) isochrones for stars below  $7 M_{\odot}$  and the Marigo et al. (2008) 3 Myr isochrone for the more massive stars as discussed in Section 3.2. The age of the cluster is first assumed to be 3 Myr and is later varied to examine the effects on the derived IMF for different cluster ages. Stars below  $\sim 3 M_{\odot}$  are on the pre-main sequence isochrone whereas the more massive stars up to our upper mass limit of  $20 M_{\odot}$  (see below) are on the main sequence. The adopted mass-luminosity relation is shown in Fig. 7.

We have limited knowledge of the extinction for the majority of our objects. Instead, we have adopted an average extinction of  $A_V = 1.85$  mag, as determined from the  $V-H$  versus  $H$  color-magnitude diagram in Fig. 6. Since the amount of extinction ranges between  $A_V = 0.7 - 3$  mag (Brandl et al. 1996) the extinction for an individual object might be wrong by up to  $A_V \sim 1$  mag, a maximum error  $< 0.2$  mag in the  $F160W$  band. This

corresponds to an error of  $\sim 10\%$  when the luminosity is transformed into a mass.

Fig. 8 shows the derived mass functions outside 0.6 pc for a 3 Myr isochrone after field stars have been subtracted statistically in each annulus. The mass functions are in general smooth and well fit by power-laws. However, there appears to be some structure in the derived IMFs at intermediate masses,  $2-4 M_{\odot}$ , which is the region where the pre-main sequence track joins the main sequence. The mass-luminosity relation is plagued by a non-monotonous feature at this mass range (see Fig. 7), which marks the radiative-convective gap (Mayne et al. 2007) and the transition region from pre-main sequence to main sequence (see also Stolte et al. 2004). A similar structure in the derived IMF is seen in the results from e.g. NGC 3603 but at a slightly higher mass since the cluster is younger (e.g. Stolte et al. 2006). The turn-on mass is higher for a younger cluster. Thus we would expect the kink in the mass-luminosity relation to move to higher masses for a younger cluster. Since this is what is seen comparing NGC 3603 and R 136, it indicates indeed a feature of the isochrones and not a feature intrinsic to the cluster. The number of stars in each mass bin is provided in Table 4.

Power-laws have been fitted to each of the histograms in order to derive the slopes of the mass function in each annulus. The fit was done over the mass range from  $20 M_{\odot}$  down to the 50% completeness limit for each annulus. The mass for stars above  $\sim 20 M_{\odot}$  is very poorly constrained from near-infrared observations due to uncertainties in the bolometric corrections (e.g. Massey 2003). The derived slopes  $\Gamma$ , where  $dN/d \log M \propto M^{\Gamma}$ , are indicated in Fig. 8 and are also presented in Table 3. The derived slopes for annuli outside 1 pc are consistent with each other within  $2\sigma$  error bars. For the 3-5 pc and 5-7 pc annuli where the data are complete to below  $2 M_{\odot}$ , the slopes are found to be  $-1.2 \pm 0.1$  and  $-0.9 \pm 0.2$ , respectively, slightly shallower than the slope of  $\Gamma = -1.28 \pm 0.05$  derived by Sirianni et al. (2000) above  $2 M_{\odot}$ , except that in our case the IMF continues as a power-law down to  $0.8 M_{\odot}$ .

Has the fact that we used the whole mass range for our power-law fit washed out a possible flattening at the low mass end? To test this possibility, we have additionally fitted a separate power-law to the low-mass part of the IMF. Only the part of the mass function that is not influenced by the kink in the mass luminosity relation is used. This region is limited to masses below  $1.7 M_{\odot}$  for the 3 Myr isochrone. It is therefore only for the 5-7 pc annulus that a reasonable mass range is covered to fit the IMF. We find the slope to be  $\Gamma = -0.9 \pm 0.2$ , which is more shallow but consistent at the  $2\sigma$  level with a Salpeter IMF and is consistent with the slope derived for the full mass range.

We have derived the IMF in the same boxes as done by Sirianni et al. (2000). The completeness correction was calculated independently for each box before the IMFs were combined to the average IMF for direct comparison with the IMF presented by Sirianni et al. (2000). The 50% completeness limit for the NICMOS data varies from  $2.8$  to  $1.4 M_{\odot}$  for the four boxes. Following Sirianni et al., we have derived an average completeness limit for the three regions of  $2.2 M_{\odot}$ . As evident, the agreement is

good for the common mass range. We appear to underestimate the stars at  $\sim 6M_{\odot}$  compared to Sirianni et al. (2000). However those appear to be recovered at  $8M_{\odot}$ .

The color–magnitude diagrams show a large spread in the main sequence to pre–main sequence transition at  $F160W=18\text{--}19$  mag. Although shown in Section 3.2 that this scatter can be explained by differential extinction, it cannot be ruled out that there is an age spread present as well as suggested in previous studies (Hunter et al. 1995; Massey & Hunter 1998). It is therefore reasonable to take a star formation history different than a single burst at 3 Myr into account. We show in Fig. 9 the IMF in the outer two annuli assuming a cluster age of 2 and 4 Myr, respectively. We also show an ‘average’ IMF found as the average of the IMF’s derived for the age range 2–4 Myr in 0.5 Myr increments. The lower mass limit in the average IMF was determined from the 4 Myr isochrone which provides the most restrictive mass limit. We find that both in the case of a 2 and 4 Myr isochrone the IMF is well fit by power–laws. The derived slopes are steeper assuming an older isochrone relative to the younger ones. There is no indication for a flattening below  $2M_{\odot}$  in either case. The average IMF is also found to be represented by a power–law with a slope consistent with a Salpeter slope. The slopes of the derived power–laws are given in Table 3. For the average IMF, the number of stars averaged over the different ages in each mass bin is derived. Error bars for the average IMF have been determined as the standard deviation around the mean number of objects in each mass bin.

As was the case for the 3 Myr isochrone, the slopes of the IMF for different assumed ages have also been calculated and are provided in Table 3. The slopes are found to be shallower than a Salpeter slope, but at the  $\sim 2\sigma$  level consistent with a Salpeter slope. The slopes are also consistent with those derived for all masses up to  $20M_{\odot}$ , as was the case assuming the 3 Myr isochrone.

The lack of a flattening in the IMF below  $2M_{\odot}$  is in contrast to the results presented by Sirianni et al. (2000), who derived the IMF closer to the cluster center. There can be several possible reasons for the difference in the derived IMF slope in the two surveys. First, due to the different spatial resolution in the two studies, the NICMOS IMF is derived further away from the center of the cluster than the WFPC2 IMF by Sirianni et al. (2000). The IMF was derived in the areas shown in Fig. 2 as regions B,C, and D. Thus, all of their surveyed area is outside a radius of 1 pc and the majority of their surveyed area is between 2 and 5 pc where crowding precludes NICMOS from detecting stars less massive than  $2.2M_{\odot}$  for a 3 Myr isochrone. One possibility for the difference in the derived slopes for the NICMOS and WFPC2 data can therefore be a variation of the IMF as a function of radius. Another possible reason can be differential extinction as suggested by Selman et al. (1999). Both possibilities are discussed in subsections 4.2 and 4.3

#### 4.2. The effect of differential extinction

As was suggested by Selman et al. (1999), the presence of differential extinction can potentially alter the low–mass end of the IMF if an extinction–limited sample is not used. In order to estimate the possible effect on the IMF if differential extinction is not taken into account, we have constructed a simple model of the clus-

ter which includes differential extinction and the depth of the dataset from Sirianni et al. (2000). A Salpeter slope IMF and a cluster age of 3 Myr were assumed. Each object within the artificial cluster was assigned a  $V$  band magnitude based on its mass from the 3 Myr isochrone computed for a half solar metallicity by Siess et al. (2000). The objects were then reddened by a foreground extinction chosen randomly from a normal distribution with a standard deviation of 0.7 and shifted to peak at  $A_V=1.85$  mag. If the extinction was found to be less than  $A_V = 0.7$  mag, a new extinction was calculated. Stars were then considered detected if their reddened magnitude is within the 50% completeness limit presented by Sirianni et al. (2000). The model is obviously an oversimplification of the real situation. Nevertheless it is expected to illustrate how the derived IMF might differ from the underlying IMF.

Figure 10 shows the input Salpeter IMF (solid line), the derived IMF (dashed line) together with the measurements by Sirianni et al. (2000). The model mimics a flattening in the observed IMF similar to that deduced by Sirianni et al. (2000). The ratio of the number of stars below and above  $2M_{\odot}$  respectively has been calculated both for the model cluster and the data from Sirianni et al. (2000). For the model cluster it is found to be 0.87, which is in reasonable agreement with the ratio of 0.76 derived from the observations.

#### 4.3. Cumulative mass functions in the outer parts of R136

Another explanation for the difference between the results obtained here and the results by Sirianni et al. (2000) can be mass segregation. We have searched for evidence for mass segregation in the two outer annuli in our survey. We used the luminosity functions instead of the mass functions to avoid additional uncertainties due to the mass–luminosity relation. The results obtained for the mass functions are very similar to those from the luminosity functions.

The cumulative luminosity distributions are shown in Fig. 11 for the outer two radial bins. These are the only bins where the 50% completeness limit is below  $2M_{\odot}$ . The two cumulative distributions are very similar. We have performed a Kolmogorov–Smirnov test to quantify the similarity of the cumulative luminosity distributions. The maximum difference between the two distributions is 0.039 and the probability for the two distributions to be drawn from the same parent distribution is 10%. Thus, there is no strong evidence (less than  $2\sigma$ ) for mass segregation in the outer parts of the cluster.

The fact that there is little evidence for mass segregation outside 3 pc does not exclude the possibility that the cluster is mass segregated out to a radius of several pc. Both Malumuth & Heap (1994) and Brandl et al. (1996) found evidence for mass segregation of the massive stars in the center of the cluster. Brandl et al. (1996) showed the half–mass relaxation time to be  $7.8\cdot 10^7$  yr, much longer than the cluster age. They also point out that the massive stars will experience mass segregation on a much shorter time scale than the lower mass stars; the time scale depends inversely on the stellar mass. It is thus not surprising, from a dynamical point of view, that there is no evidence for mass segregation outside the half–mass radius of 1.7 pc (Hunter et al. 1995).

On the other hand, this does not rule out the possibility that the cluster might be mass segregated at birth closer to the cluster center. Evidence for mass segregation has been found in e.g. the Orion Nebula Cluster (ONC) (Hillenbrand & Hartmann 1998; Bonnell & Davies 1998). Hillenbrand & Hartmann (1998) showed evidence for mass segregation down to stellar masses of  $1\text{--}2 M_{\odot}$ . Due to the youth of the ONC, they concluded the mass segregation had to be at least partly primordial. It is thus possible that R136 is also affected by primordial mass segregation close to the cluster center and that mass segregation is the reason for the difference between the NICMOS and WFPC2 IMFs.

#### 4.4. Cluster mass

We can obtain a rough estimate of the cluster mass from the near-infrared observations. The main limitation in our mass estimate is the amount of confusion due to crowding in the cluster centre: our data mainly samples the IMF down to and below  $1.4 M_{\odot}$  outside 3 pc. Nevertheless, we can utilise the mass estimates within 2 pc from Hunter et al. (1995) to complement our mass estimate down to  $2.1 M_{\odot}$ . Inside 2 pc and into 0.15 pc, the results are extrapolated from the local completeness limit mass down to  $2.1 M_{\odot}$  assuming an underlying Salpeter IMF. No stars have been detected less massive than  $20 M_{\odot}$  within the central 0.15 pc radius due to crowding. The mass in the very center has been estimated from the surface density profile down to  $2.8 M_{\odot}$  in Hunter et al. (1995) to be  $4 \cdot 10^4 M_{\odot} \text{pc}^{-2}$ , resulting in a mass of  $3700 M_{\odot}$  down to a lower mass limit of  $2.1 M_{\odot}$ . We find the cluster total mass down to  $2.1 M_{\odot}$  to be  $5 \cdot 10^4 M_{\odot}$ . The directly determined mass down to  $2.8 M_{\odot}$  within 4.7 pc is found to be  $2.0 \cdot 10^4 M_{\odot}$ , almost the same as found by Hunter et al. (1995). If the IMF follows a Salpeter slope down to  $0.5 M_{\odot}$  as observed in the Galactic field and nearby lower-mass clusters (Kroupa 2002), the total mass in the central region would be roughly double the amount given above, and the total cluster mass would be close to  $\sim 10^5 M_{\odot}$ .

The velocity dispersion, and hence the dynamical mass, of the whole NGC 2070 region, including R 136 has been determined by Bosch et al. (2009). The dynamical mass was determined to be  $4.5 \cdot 10^5 M_{\odot}$ , almost 5 times higher than expected for R 136 alone, but consistent with the photometric mass for the same area (Selman et al. 1999). If we take into account that the half mass radius of R 136 is 1.7 pc (Hunter et al. 1995), compared to 14 pc for the whole NGC 2070 region and assuming the velocity dispersion is the same in the inner parts of the cluster, we would expect a dynamical mass of  $4.5 \cdot 10^5 \cdot 1.7/14 M_{\odot} = 5.5 \cdot 10^4 M_{\odot}$  which is lower than the mass expected if the IMF is consistent with a Galactic IMF down to  $0.5 M_{\odot}$ . Thus, at face value, the velocity dispersion would be low enough that the cluster can stay bound. However, a measurement of the velocity dispersion for the inner regions is necessary to directly compare the photometric mass with the dynamical mass.

#### 4.5. The surface brightness profile

We can directly derive the surface brightness profile of the region around R136 in the 30 Dor cluster since the data does not suffer from saturated stars. Although

bright stars will saturate through the one hour exposure, the non-destructive readout mode ensures that only the first reads are used to derive the magnitude of the brightest stars. The surface brightness profile is shown in Fig. 12.

Between  $\sim 0.2$  and 2 pc, the light profile is well fit by a power-law, whereas inside 0.2 pc the light profile appears to be flattening. We have therefore fitted the light profile with a power-law modified by a core radius, similar to the approach in Elson et al. (1987). Constraining the fit to inside 2 pc, we find a slope of  $-1.54 \pm 0.02$ , slightly more shallow than  $-1.72 \pm 0.06$  derived outside 0.1 pc by Campbell et al. (1992) using *F336W* Planetary Camera onboard HST observations.

The core radius is found to be  $0.025 \pm 0.004 \text{pc}$ , which is less than the resolution of the observations and is thus likely and upper limit. Previous HST optical studies determined a small core radius,  $r_c \leq 0.02 \text{pc}$  (Hunter et al. 1995), consistent with our findings here. However, since the derived core radius is smaller than the resolution of the observations, it's evidence is weak. One or two bright stars off center by only a small amount could mimic a cluster core.

#### 4.6. Comparison with other massive clusters and the implications of low-mass stars in R136

How does the low-mass end of the IMF in 30 Dor compare with that determined for other massive and dense stellar clusters? A top-heavy IMF in massive dense clusters has been suggested on theoretical grounds (e.g. Silk 1995). The most convincing example of a young cluster with a present-day mass function departing significantly from a Salpeter IMF above  $1 M_{\odot}$  is the Arches cluster (Stolte et al. 2002; Figer et al. 1999). Stolte et al. (2002) found an average slope of  $\Gamma = -0.9 \pm 0.15$  for the central parsec of the Arches cluster, flatter than a Salpeter slope of -1.35. Deeper observations found that the present day mass function in Arches to be well approximated by a power-law with a slope of  $\Gamma = -0.91 \pm 0.08$  down to  $1.3 M_{\odot}$  (Kim et al. 2006). However, recent work taking differential extinction into account suggest the slope of the power-law is only slightly more shallow than a Salpeter slope,  $\Gamma = -1.1 \pm 0.2$  (Espinoza et al. 2009). Portegies Zwart et al. (2002) note that even if the observed IMF is slightly flatter than a Salpeter IMF, this can be explained by mass segregation. The mass segregation would be accelerated in the cluster due to the strong gravitational field from the Galactic Center. By adopting realistic parameters for a model cluster and an appropriate distance from the Galactic center, they found that an input Salpeter slope IMF would be transformed to the observed present day mass function via strong dynamical evolution. Stolte et al. (2006) showed that the IMF of the cluster powering the NGC 3603 HII region was well fitted by a power-law but with a slope flatter than Salpeter,  $\Gamma = -0.91 \pm 0.15$ . They further showed evidence for mass segregation for the more massive stars,  $M > 4 M_{\odot}$ . The data indicated a slight flattening of the low-mass content ( $M < 3 M_{\odot}$ ). NGC 3603 is younger than the Arches cluster and not affected by a strong tidal gravitational field. Thus it is expected to be less influenced by dynamical mass segregation.

The even more massive starburst clusters appear to be the primary sites (unit cells) of star formation in star-



burst galaxies, including interacting/colliding galaxies such as The Antennae or The Cartwheel. If starburst clusters are the basic building blocks of certain star-forming galaxies, their stellar content (IMF) will affect much of the observed chemical and photometric evolution of galaxies, both at the present epoch and perhaps even more so in the high-redshift past (Charlot et al. 1993). Several observational claims have been made that the IMF in unresolved starburst clusters is top-heavy (Rieke et al. 1993), although observations of the Antennae gave a mixed result (Mengel et al. 2002). However, it has been suggested that the high mass-to-light ratios found in some young starburst clusters are artificially high related to their not being in virial equilibrium due to gas expulsion from the clusters (Goodwin & Bastian 2006). During the first 50 Myr of the cluster, the velocity dispersion and hence the cluster mass might be overestimated if the cluster is assumed to be virialized. Goodwin & Bastian (2006) suggest that the top-heavy IMFs inferred in young unresolved extragalactic star clusters might be spurious due to their non-virialized dynamical state.

With the present dataset it is clear that the IMF in the outer parts of R136 continues as a power-law down to  $1 M_{\odot}$ , similar to what is found in other star clusters and the slope is similar to what is found in the field. Whether this is true for the cluster as a whole depends on the cause for the flattening observed closer to the cluster center. It would be interesting to know the IMF if the observations could be extended closer to the characteristic mass where the Galactic field star IMF flattens ( $0.5 M_{\odot}$  Kroupa 2002), a mass that can be reached in massive young clusters ( $\leq 4$  Myr) in the LMC with AO systems.

It has long been suggested R136 might be a proto-globular cluster (Meylan 1993; Larson 1993). The question has been whether R136 would remain bound over a Hubble time. One consequence of a top-heavy IMF is that the cluster would dissolve soon after gas expulsion and mass loss due to evolution of the high-mass stars. However, the detection of stars in R136 less massive than  $1 M_{\odot}$  gives the first *direct* evidence that low-mass stars are formed in a starburst cluster. The fact that the IMF in the outer parts of R136 appears to be a Salpeter IMF down to at least  $1 M_{\odot}$  gives support to the notion the cluster might be a proto-globular cluster, albeit a light one. Early gas expulsion and subsequent mass loss through stellar evolution will disrupt star clusters deficient in low-mass stars during the first 5 Gyr of the clusters life (Chernoff & Weinberg 1990; Goodwin 1997) However, a determination of the velocity dispersion in the inner parts of the cluster is necessary to determine its final fate. Thus, the presence of low-mass stars is a necessary, but not sufficient condition for the possibility of the cluster to evolve into a globular cluster. The median mass of Galactic globular clusters is  $8.1 \cdot 10^4 M_{\odot}$  (Mandushev et al. 1991), comparable to the mass of R136. Even if R 136 will remain bound it will lose some mass and might end up as a low-mass globular cluster.

## 5. CONCLUSIONS

We have analyzed HST/NICMOS *F160W* band data covering the central  $14\text{pc} \times 14.25\text{pc}$  around R136 in the NGC 2070 cluster in the LMC. We have reached the fol-

lowing conclusions:

- From the color-magnitude diagram obtained by combining our photometry with previously published HST/WFPC 2 *F555W* data we constrain the age of the lower-mass stellar content in the cluster to be 2–4 Myr, consistent with previous estimates. We derive individual masses for the objects detected adopting a 3 Myr isochrone.
- We have detected stars in the cluster down to  $0.5 M_{\odot}$  at  $r > 5$  pc, assuming an age of 3 Myr.
- The derived IMF is consistent with a Salpeter slope IMF with no evidence for a flattening at low masses down to the 50% completeness limit corresponding to a mass of  $1.1 M_{\odot}$  outside a radius of 5 pc for a 3 Myr population and  $1.4 M_{\odot}$  if the oldest stars are 4 Myr.
- The result is in disagreement with the flattening of the IMF below  $2 M_{\odot}$  observed by Sirianni et al. (2000) using optical data covering a region closer to the cluster center. We suggest two possible reasons for the discrepancy: differential extinction and mass segregation.
- We find no evidence for mass segregation outside 3 pc, but with the current data, we cannot rule out that closer to the center the low-mass stars are segregated.
- From the radial surface brightness profile we have derived a core radius for the cluster of  $0.025$  pc ( $0''.1$ ), consistent with previous estimates by Hunter et al. (1995).
- The mass of the cluster within 7 pc between  $25 M_{\odot}$  and down to  $2.1 M_{\odot}$  is estimated to be  $5 \cdot 10^4 M_{\odot}$ . If the IMF continues with a Salpeter slope down to  $0.5 M_{\odot}$  the total mass estimate will double.
- The total mass of the cluster combined with the large number of low-mass stars suggests that the 30 Dor cluster may survive to become a proto-globular cluster depending on the cluster velocity dispersion.

We thank Richard Larson for discussions in the early phases of the project, Eddie Bergeron for assistance with the drizzle software, and Matthew Kenworthy for commenting on an early version of the manuscript. M. A. and H. Z. acknowledges support from the DLR grant 50OR9912: “Data analysis of NICMOS/HST images of the 30 Dor cluster” and partial funding through the DLR grant 50OR0401. M.A thanks the Astrophysikalisches Institut Potsdam for providing a stimulating and supportive environment for carrying out this Thesis work. Additional support was funded through the European Commission Fifth Framework Programme Research Training Network “The Formation and Evolution of Young Stellar Clusters” (HPRN-CT-2000-00155). The Astronomische Gesellschaft is acknowledged for providing funding for travel. Support for this work was provided by NASA through grant number GO-07370.01-96A

from the Space Telescope Science Institute, which is operated by the Association of Universities for Research in Astronomy, Inc., under NASA contract NAS 5-26555.

Facilities: This paper is based on observations made with the NASA/ESA *Hubble Space Telescope*, operated

by the Space Telescope Science Institute, which is operated by the Association of Universities for Research in Astronomy, Inc., under NASA contract NAS5-26555.

## REFERENCES

- Andersen, M. 2005, PhD Thesis, University of Potsdam, Germany
- Andersen, M., Meyer, M. R., Greissl, J., Oppenheimer, B. D., Kenworthy, M. A., McCarthy, D. W., & Zinnecker, H. 2005, IAU Symposium, 227, 285, Cambridge University Press, Eds. R. Cesaroni, E. Churchwell, M. Felli, & C.M. Walmsley.
- Andersen, M., Meyer, M. R., Greissl, J., & Aversa, A. 2008, *ApJ*, 683, L183
- Bonnell, I. A., & Davies, M. B. 1998, *MNRAS*, 295, 691
- Bosch, G., Terlevich, E., & Terlevich, R. 2009, *AJ*, 137, 3437
- Brandl, B., et al. 1996, *ApJ*, 466, 254
- Brandner, W., Grebel, E. K., Barbá, R. H., Walborn, N. R., & Moneti, A. 2001, *AJ*, 122, 858
- Campbell, B., et al. 1992, *AJ*, 104, 1721
- Cassinelli, J. P., Mathis, J. S., & Savage, B. D. 1981, *Science*, 212, 1497
- Chabrier, G. 2005, *The Initial Mass Function 50 Years Later*, 327, 41
- Charlot, S., Ferrari, F., Mathews, G. J., & Silk, J. 1993, *ApJ*, 419, L57
- Chernoff, D. F., & Weinberg, M. D. 1990, *ApJ*, 351, 121
- de Marchi, G., Nota, A., Leitherer, C., Ragazzoni, R., & Barbieri, C. 1993, *ApJ*, 419, 658
- Eisenhauer, F., Quirrenbach, A., Zinnecker, H., & Genzel, R. 1998, *ApJ*, 498, 278
- Elson, R. A. W., Fall, S. M., & Freeman, K. C. 1987, *ApJ*, 323, 54
- Espinoza, P., Selman, F. J., & Melnick, J. 2009, *A&A*, 501, 563
- Figer, D. F., Kim, S. S., Morris, M., Serabyn, E., Rich, R. M., & McLean, I. S. 1999, *ApJ*, 525, 750
- Goodwin, S. P. 1997, *MNRAS*, 284, 785
- Goodwin, S. P., Whitworth, A. P., & Ward-Thompson, D. 2004, *A&A*, 423, 169
- Goodwin, S. P., & Bastian, N. 2006, *MNRAS*, 373, 752
- Gürkan, M. A., Freitag, M., & Rasio, F. A. 2004, *ApJ*, 604, 632
- Hillenbrand, L. A., & Hartmann, L. W. 1998, *ApJ*, 492, 540
- Hook, R., & Krist, J. 1997, *Space Telescope European Coordinating Facility Newsletter*, Volume 24, p.10, 24, 10
- Holtzman, J. A., Burrows, C. J., Casertano, S., Hester, J. J., Trauger, J. T., Watson, A. M., & Worthey, G. 1995, *PASP*, 107, 1065
- Hunter, D. A., Shaya, E. J., Holtzman, J. A., Light, R. M., O'Neil, E. J., & Lynds, R. 1995, *ApJ*, 448, 179
- Hunter, D. A., O'Neil, E. J., Lynds, R., Shaya, E. J., Groth, E. J., & Holtzman, J. A. 1996, *ApJ*, 459, L27
- Kennicutt, R. C., Jr. 1984, *ApJ*, 287, 116
- Kim, S. S., Figer, D. F., Kudritzki, R. P., & Najarro, F. 2006, *ApJ*, 653, L113
- Kroupa, P. 2002, *Science*, 295, 82
- Lada, C. J., & Lada, E. A. 2003, *ARA&A*, 41, 57
- Larson, R. B. 1993, *ASP Conf. Ser.* 48: *The Globular Cluster-Galaxy Connection*, 48, 675 *Astronomical Society of the Pacific (ASP)*, edited by Graeme H. Smith, and Jean P. Brodie
- Larson, R. B. 1998, *MNRAS*, 301, 569
- Low, C., & Lynden-Bell, D. 1976, *MNRAS*, 176, 367
- Maercker, M., & Burton, M. G. 2005, *A&A*, 438, 663
- Malumuth, E. M., & Heap, S. R. 1994, *AJ*, 107, 1054
- Mandushev, G., Staneva, A., & Spasova, N. 1991, *A&A*, 252, 94
- Marigo, P., Girardi, L., Bressan, A., Groenewegen, M. A. T., Silva, L., & Granato, G. L. 2008, *A&A*, 482, 883
- Massey, P. 2003, *ARA&A*, 41, 15
- Massey, P., Lang, C. C., Degioia-Eastwood, K., & Garmany, C. D. 1995, *ApJ*, 438, 188
- Massey, P., & Hunter, D. A. 1998, *ApJ*, 493, 180
- Mayne, N. J., Naylor, T., Littlefair, S. P., Saunders, E. S., & Jeffries, R. D. 2007, *MNRAS*, 375, 1220
- McGregor, P. J., & Hyland, A. R. 1981, *ApJ*, 250, 116
- Megeath, S. T. 1996, *A&A*, 311, 135
- Melnick, J. 1985, *A&A*, 153, 235
- Mengel, S., Lehnert, M. D., Thatte, N., & Genzel, R. 2002, *A&A*, 383, 137
- Meylan, G. 1993, *ASP Conf. Ser.* 48: *The Globular Cluster-Galaxy Connection*, 48, 588, *Astronomical Society of the Pacific (ASP)*, edited by Graeme H. Smith, and Jean P. Brodie
- Meyer, M. R., Adams, F. C., Hillenbrand, L. A., Carpenter, J. M., & Larson, R. B. 2000, *Protostars and Planets IV*, 121
- Muench, A. A., Lada, E. A., Lada, C. J., & Alves, J. 2002, *ApJ*, 573, 366
- Najarro, F., Figer, D. F., Hillier, D. J., & Kudritzki, R. P. 2004, *ApJ*, 611, L105
- Omukai, K. 2000, *ApJ*, 534, 809
- Parker, J. W. 1993, *AJ*, 106, 560
- Pehlemann, E., Hofmann, K.-H., & Weigelt, G. 1992, *A&A*, 256, 701
- Portegies Zwart, S. F., Makino, J., McMillan, S. L. W., & Hut, P. 2002, *ApJ*, 565, 265
- Rieke, G. H., Loken, K., Rieke, M. J., & Tamblyn, P. 1993, *ApJ*, 412, 99
- Robberto, M., Song, J., Mora Carrillo, G., Beckwith, S. V. W., Makidon, R. B., & Panagia, N. 2004, *ApJ*, 606, 952
- Rubio, M., Roth, M., & Garcia, J. 1992, *A&A*, 261, L29
- Salpeter, E. E. 1955, *ApJ*, 121, 161
- Selman, F., Melnick, J., Bosch, G., & Terlevich, R. 1999, *A&A*, 341, 98
- Siess, L., Dufour, E., & Forestini, M. 2000, *A&A*, 358, 593
- Silk, J. 1995, *ApJ*, 438, L41
- Sirianni, M., Nota, A., Leitherer, C., De Marchi, G., & Clampin, M. 2000, *ApJ*, 533, 203
- Smith, V. V. 1999, *IAU Symp.* 190: *New Views of the Magellanic Clouds*, 190, 259, *The Astronomical Society of the Pacific*, Edited by Y.-H. Chu, N. Suntzeff, J. Hesser, & D. Bohlender
- Spitzer, L. 1987, Princeton, NJ, Princeton University Press, 1987
- Stolte, A., Grebel, E. K., Brandner, W., & Figer, D. F. 2002, *A&A*, 394, 459
- Stolte, A., Brandner, W., Brandl, B., Zinnecker, H., & Grebel, E. K. 2004, *AJ*, 128, 765
- Stolte, A., Brandner, W., Brandl, B., & Zinnecker, H., 2006, *AJ*, 132, 253
- Walborn, N. R., & Blades, J. C. 1997, *ApJS*, 112, 457
- Weigelt, G., & Baier, G. 1985, *A&A*, 150, L18
- Westerlund, B. E. 1997, *The Magellanic Clouds*, Cambridge University Press
- Zinnecker, H., Brandl, B., Brandner, W., Moneti, A., & Hunter, D. 1999, *IAU Symp.* 190: *New Views of the Magellanic Clouds*, 190, *The Astronomical Society of the Pacific*, Edited by Y.-H. Chu, N. Suntzeff, J. Hesser, & D. Bohlender
- Zinnecker, H., Andersen, M., Brandl, B., Brandner, B., Hunter, D., Larson, R., McCaughrean, M. J., Meylan, G., & Moneti, A. 2002, *IAU Symp.* 207: *Extragalactic Star Clusters*, 531, San Francisco: *Astronomical Society of the Pacific*, Edited by D. Geisler, E.K. Grebel, and D. Minniti.

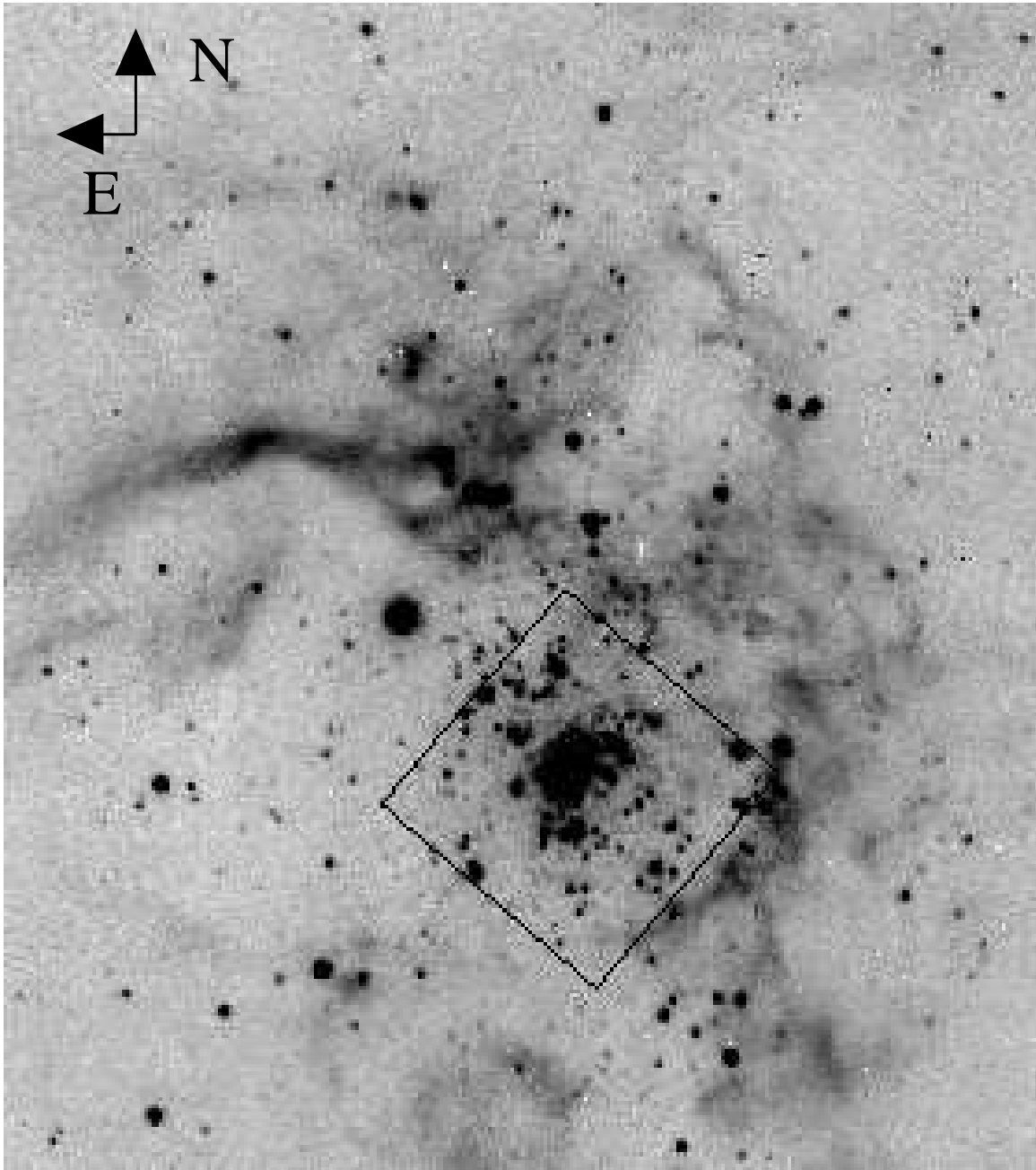


FIG. 1.— Location of the NICMOS surveyed region within 30 Dor, outlined by the black box, overlaid on a  $K$  band image obtained with the IRAC-2a camera on the MPI/ESO 2.2 meter telescope (see Brandner et al. 2001, for details). The full field is  $200'' \times 225''$  and the NICMOS field is  $56'' \times 57''$ . North is up and East is left.

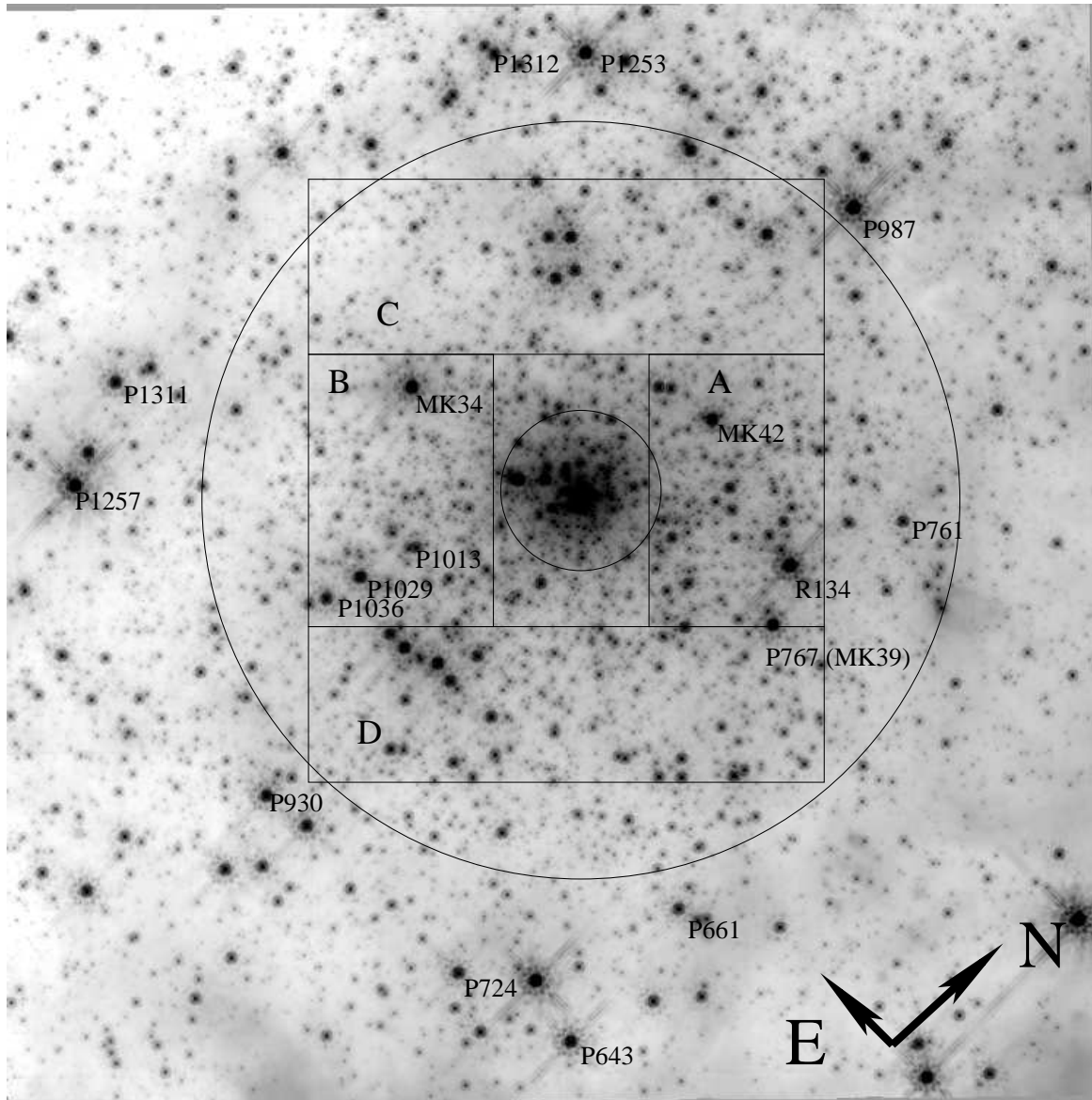


FIG. 2.— The central region around R136 in the 30 Dor cluster (NGC 2070) as observed through the  $F160W$  filter with the NICMOS Camera 2 on HST. The field-of-view is  $56'' \times 57''$ , corresponding to  $14 \text{ pc} \times 14.25 \text{ pc}$ . A logarithmic inverted intensity scale has been used. North and East are indicated in the Figure. The faintest sources visible in the image are  $F160W \sim 21.5$  mag. Stars with spectral types determined by Parker (1993) are marked by their ID number, along with R134, MK34, and MK42 (Melnick 1985) to the lower right of each star. All the identified stars are early O or WR type stars, except P1257 (B0IA), P1253 (BN0.5Ia), and P987 (B0.5–0.7I). The spectral types are adopted from Walborn & Blades (1997). The four regions analysed by Sirianni et al. (2000) are shown and labeled. Further, the 1 pc and 5 pc radii are indicated by circles.

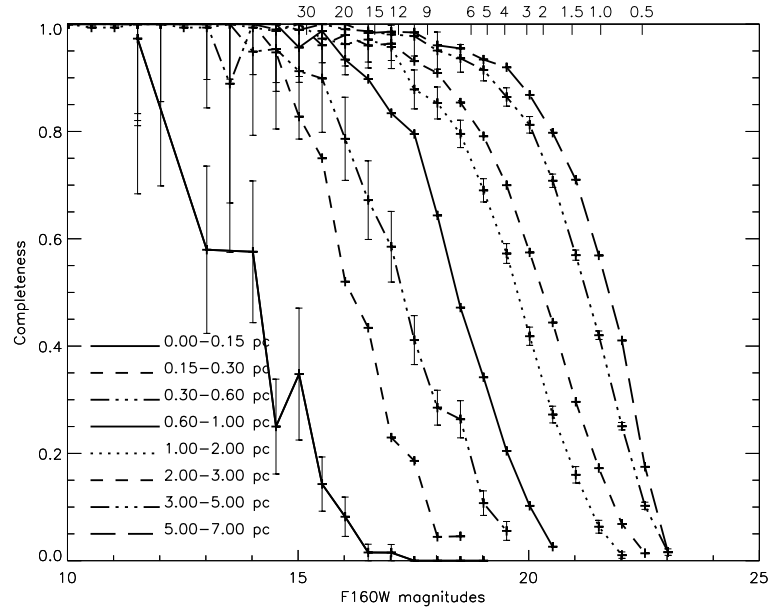


FIG. 3.— The completeness as a function of magnitude for different annuli extending from the center to the edge of the field. The error bars indicated on every second curve are the statistical fluctuations in the completeness tests. The corresponding masses for a 3 Myr isochrone and an extinction of  $A_V = 1.85$  mag are indicated at the top of the plot.

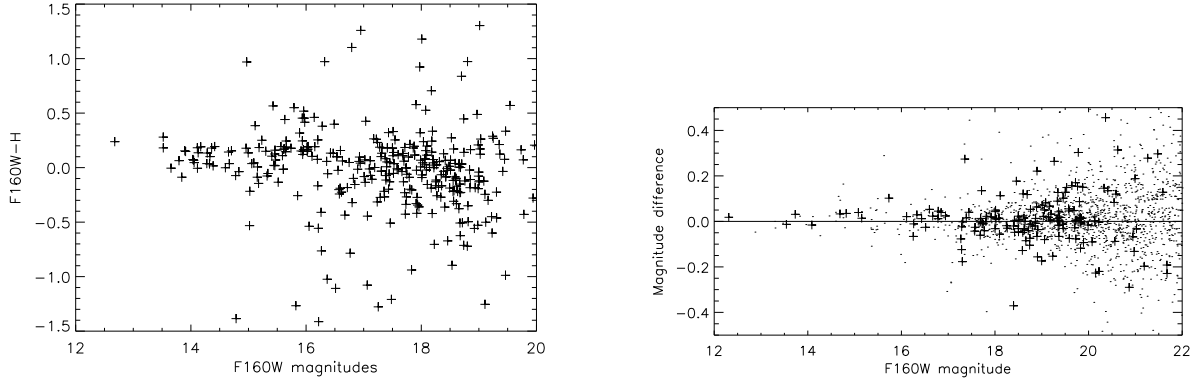


FIG. 4.— Left: A comparison of the NICMOS 2 photometry derived in this study with the ground-based AO  $H$  band observations by Brandl et al. (1996). The mean difference between the two datasets for objects with  $F160W \leq 17$  mag is 0.03 mag, and the standard deviation is 0.2 mag. Right: The magnitude difference for sources detected in two different images in the mosaic. A star was identified in both images if its position was within one pixel. Plus signs denote stars within a 2 pc radius of the center, but outside 1.25 pc; the dots denote stars outside this annulus. The RMS in the error for objects with  $F160W < 21.5$  mag, which is the 50% completeness limit in the outskirts of the cluster, is 0.17 mag.

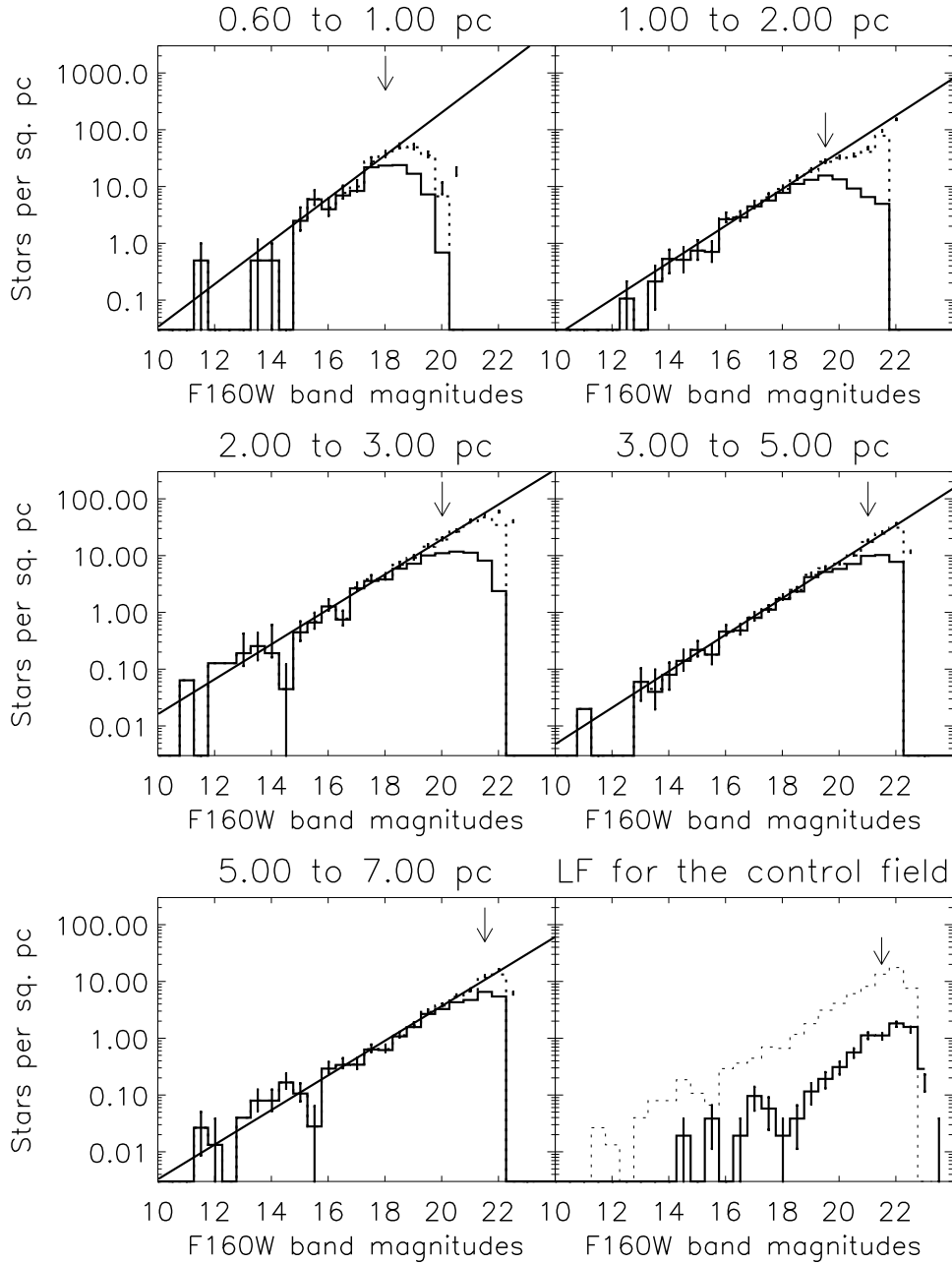


FIG. 5.— The  $F160W$ -band luminosity functions for different annuli in R136 outside a radius of 0.6 pc. Solid histograms indicate the observed number of stars per magnitude bin while the completeness-corrected data are shown as the dotted lined histograms. The error bars include the Poisson errors and the uncertainty from the incompleteness calculations where the two error terms have been added in quadrature. In each panel, an arrow indicates the bin where the completeness correction is 50%. The solid straight line is a weighted fit to the completeness corrected histograms down to the 50% completeness limit. The lower right panel shows the completeness corrected average luminosity function for the two control fields (solid histogram) associated with the 30 Dor cluster. The completeness corrected luminosity function for the 5–7 pc annulus in 30 Dor is shown as the dashed histogram for comparison.

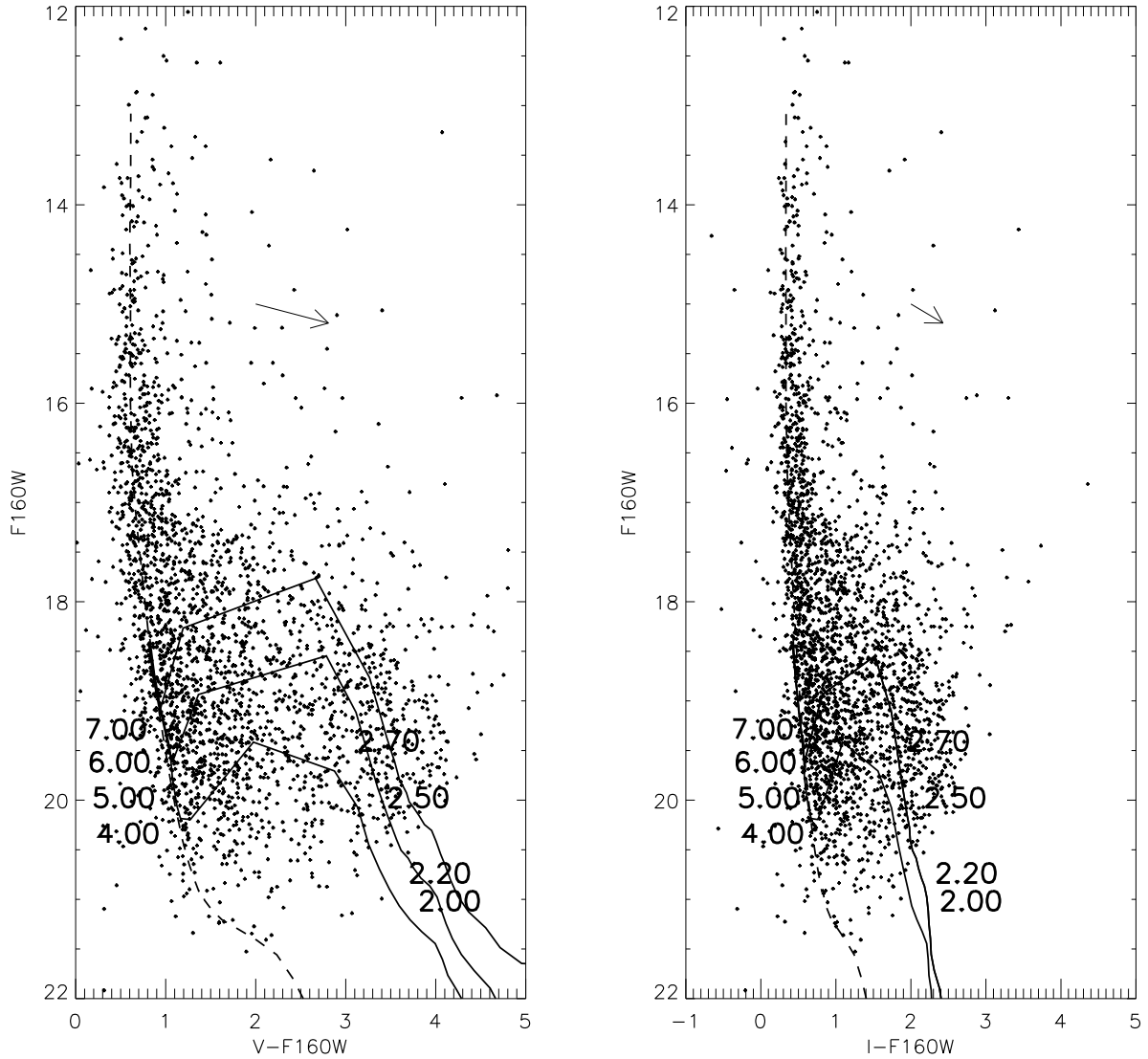


FIG. 6.— Left: The  $F555W-F160W$  versus  $F160W$  color-magnitude diagram for R136 for the central  $35'' \times 35''$  observed by Hunter et al. (1995) in the  $F555W$  and  $F814W$  bands. The arrow illustrates the effect of  $A_V = 1$  mag of extinction ( $A_{F160W} = 0.175 \times A_V$ ). Overplotted as the solid lines are the 2, 3, and 4 Myr pre-main sequence isochrones from Siess et al. (2000) below  $7 M_\odot$ . The long dashed line is the main sequence from Marigo et al. (2008) below  $7 M_\odot$  and the 3 Myr isochrone from a Marigo et al. (2008) above  $7 M_\odot$ . All the isochrones have been reddened by  $A_V = 1.85$  mag, the median reddening for the high mass stars (see the text) and shifted by a distance modulus of 18.5. The  $F555W$  magnitudes have been transformed into the  $V$  magnitude using the transformations in Holtzman et al. (1995). The 3 Myr Siess et al. (2000) isochrone joins the main sequence at  $F160W \sim 19.5$  mag,  $V-F160W = 0.8$  mag. Masses are indicated on the 2 Myr isochrone. Right: Same as to the left but this time the  $I-F160W$  versus  $F160W$  color-magnitude diagram. Notice the tighter clustering around the isochrone to the right, indicating part of the scatter in the  $V-F160W$  color-magnitude diagram is due to differential reddening.



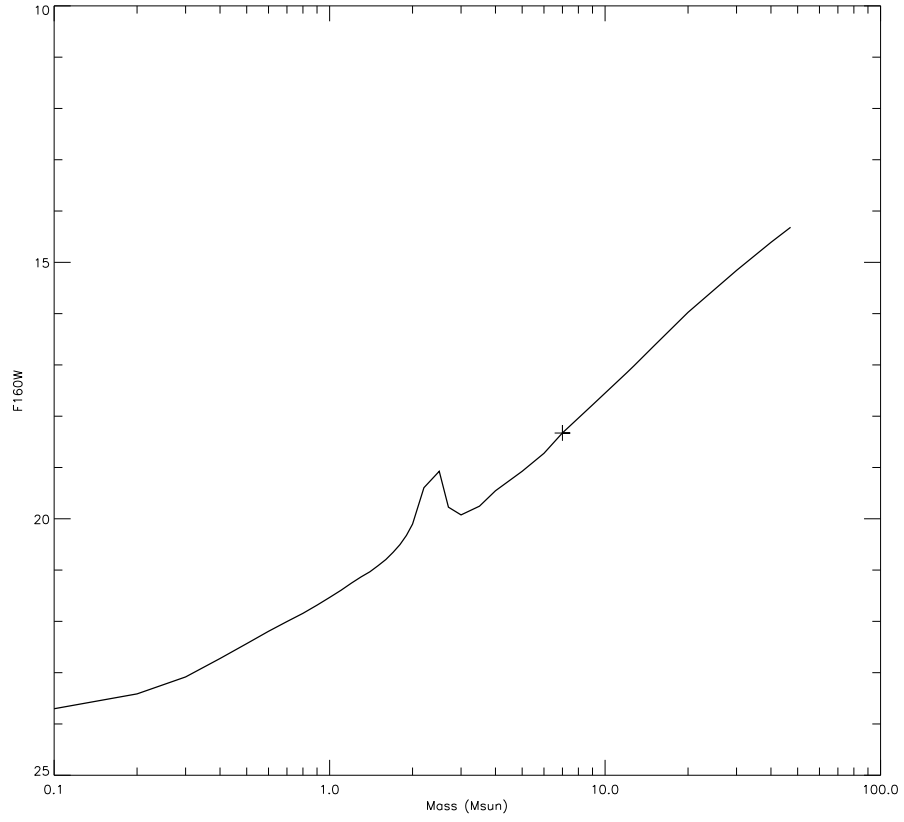


FIG. 7.— The mass–luminosity relation for a 3 Myr isochrone. Marked is the location where the Siess et al. (2000) and Marigo et al. (2008) isochrones merge ( $7 M_{\odot}$ ). The feature at 2–3  $M_{\odot}$  is due to the pre-main sequence to main sequence transition.

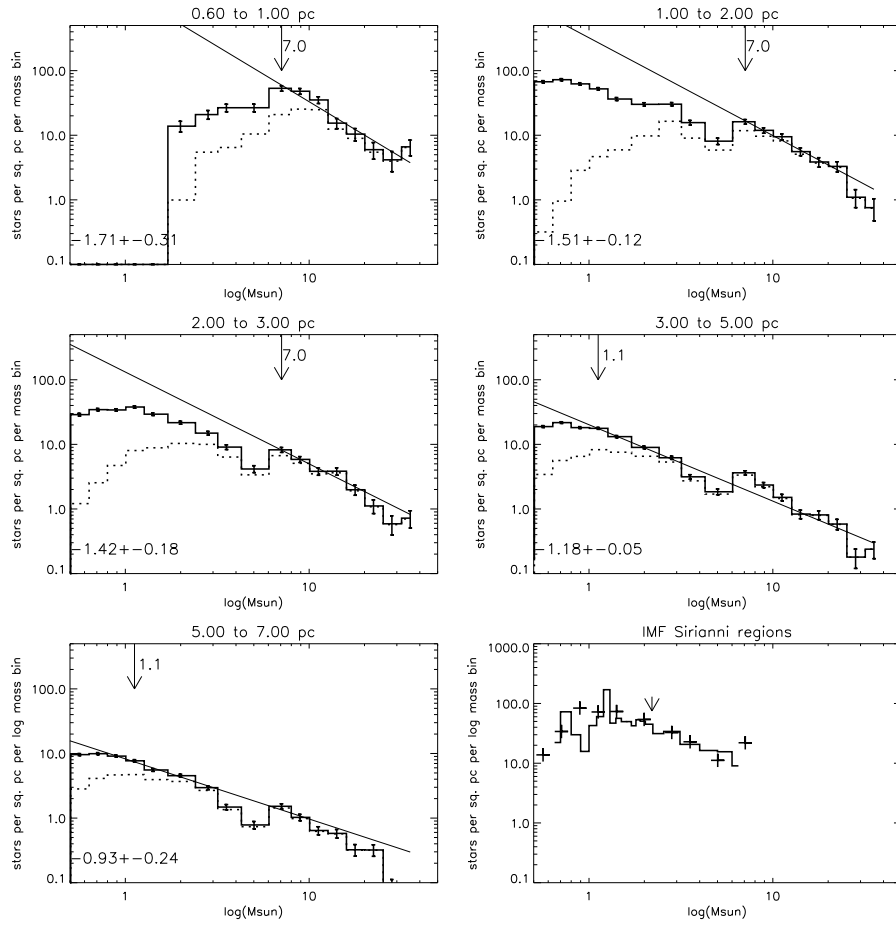


FIG. 8.— The mass functions for 30 Dor outside 0.6 pc in several annuli after field star subtraction. The arrows indicate the 50% completeness limit. Dotted line histograms show the mass functions derived from the uncorrected star counts whereas the solid line histograms are the completeness corrected mass function. Expected errors due to Poisson noise are indicated on the solid line histograms. A fit is made to the completeness corrected histogram, corrected for field star contamination. The maximum mass used in the fits is  $20 M_{\odot}$ . The coefficient shown in each panel is  $\Gamma$ ,  $dN/d\log M \propto M^{\Gamma}$ . The lower right panel shows the IMF derived by Sirianni et al. (2000) from the areas shown in Fig. 2. Further, the plus symbols show the IMF derived from the NICMOS data from the same regions as was used in the Sirianni et al. (2000) study. The 50% completeness is  $2 M_{\odot}$  for this sample, as shown by the arrow.

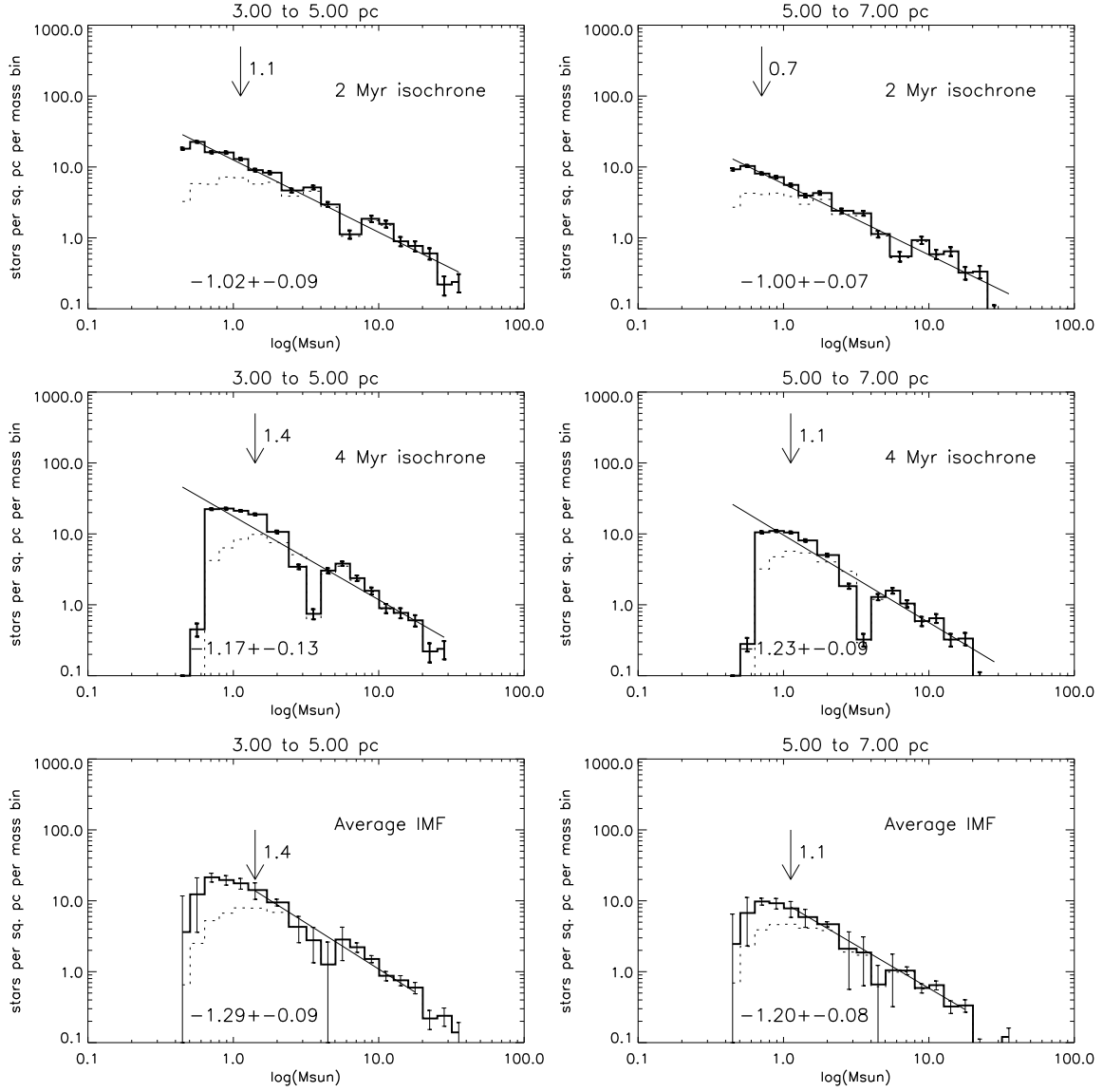


FIG. 9.— The derived IMF’s between 3–7 pc assuming a 2 Myr isochrone (top), a 4 Myr isochrone (middle) and an average of the IMF’s derived for the 2 to 4 Myr isochrones in 0.5 Myr increments (bottom). The error bars on the top two panels include Poisson noise and the uncertainties in the completeness corrections. The number of stars in each mass bin in the average IMF is determined as the average of the 5 IMF’s for ages 2–4 Myr. The error bars for each bin in the average IMF are then calculated as the standard deviation of the number of stars in the bin. The arrow shows the 50% completeness limit in each panel and the number next to arrow indicate the limiting mass in solar masses. For the average IMF, the 50% completeness limit is determined by the 4 Myr isochrone since here the completeness limit corresponds to the highest mass.

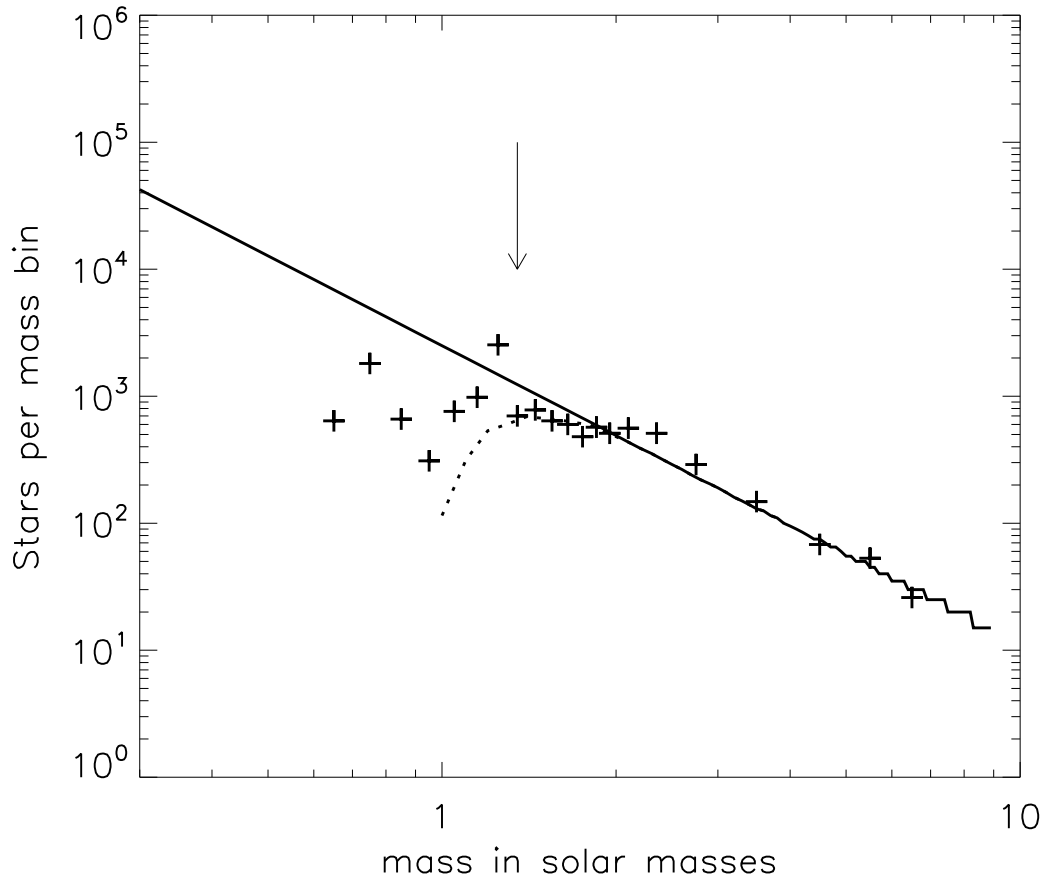


FIG. 10.— An illustration of the effect on the derived IMF of individual random differential extinction within 30 Dor. The solid line is an artificial Salpeter mass function and the dotted line is the retrieved mass function by adopting a magnitude-limited sample. The magnitude limit was assumed to be the same as used by Sirianni et al. (2000) ( $V=24.7$  mag). Crosses show the mass function derived by Sirianni et al. (2000). The stair-case shape of the input IMF at the high-mass end is due to finite, yet constant size of the mass bins. The 50% completeness limit at  $1.35 M_{\odot}$  is indicated by the arrow.

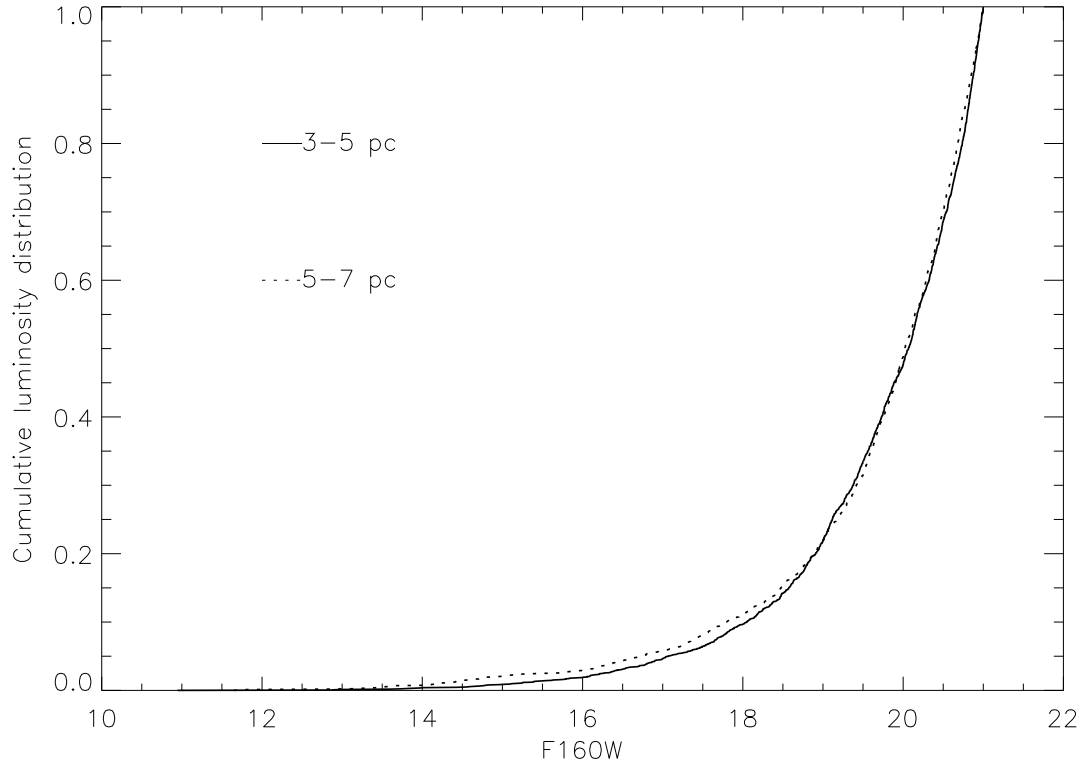


FIG. 11.— A comparison of two cumulative luminosity distributions outside 3 pc and down to the 50% completeness level of  $F160W = 21$  mag for the 3–5 pc annulus. A K–S test of the two distributions gives a maximum distance between the two distributions of 0.039 and the probability the two distributions to be drawn from the same parent distribution is 10%. The implication is that there is no evidence for luminosity segregation in the two annuli.

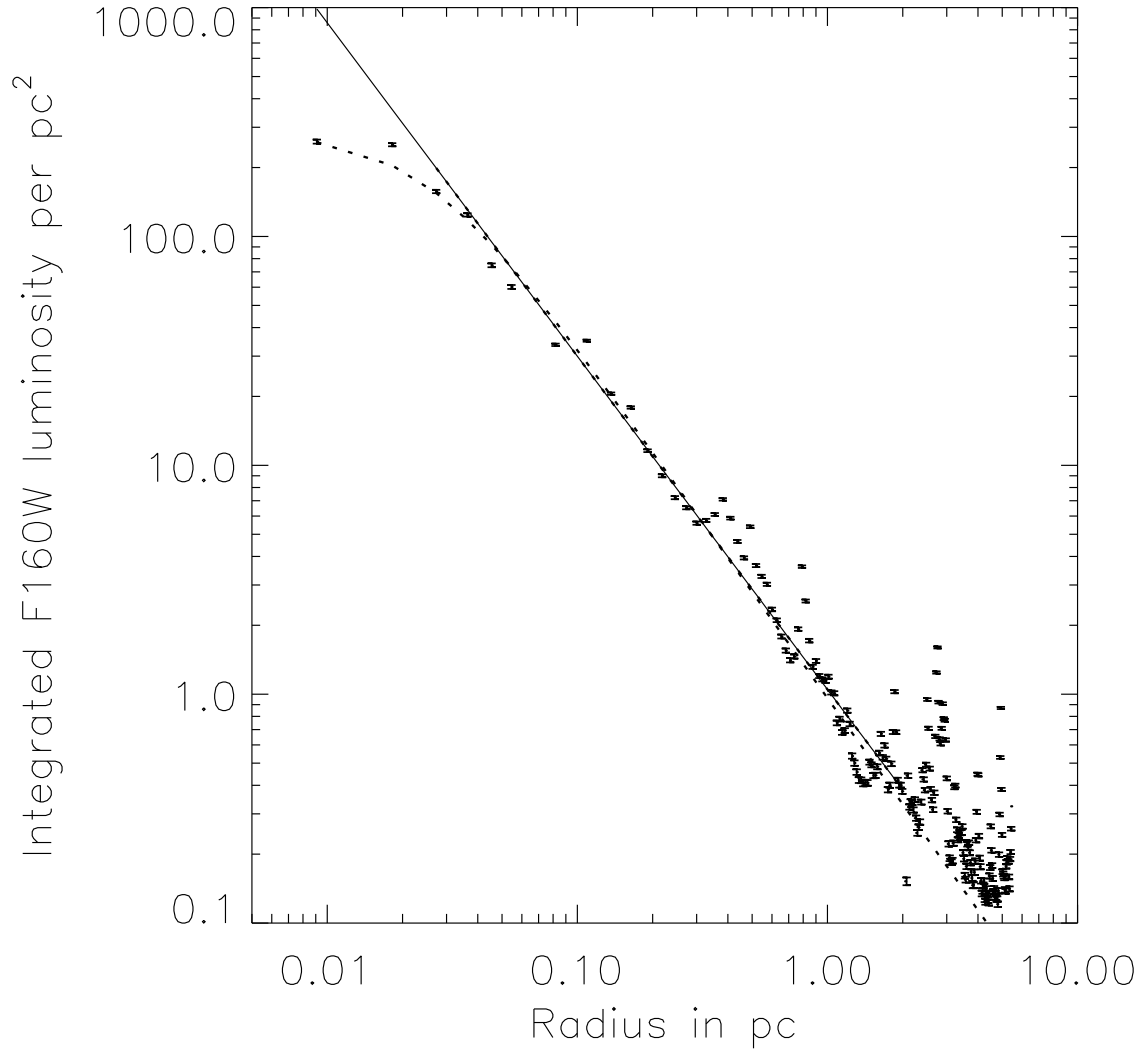


FIG. 12.— The surface brightness profile of the R136 cluster within a 7 pc radius of the cluster center. The solid line is a pure power-law fit from 0.02 pc to 2 pc with a derived slope of  $-1.48$ . The dashed line is an Elson, Fall & Freeman type profile with a core radius of 0.025 pc and a power-law slope of  $-1.54$ . The fit was done from 0.009 pc–2 pc. Beyond 2 pc, the presence of the individual bright stars labeled in Fig. 2 introduces the jitter seen in the surface brightness profile.

Annulus(pc)	slope( $\alpha$ )	Max( $F160W$ )
0.6 – 1.0	$0.38 \pm 0.07$	18.0
1.0 – 2.0	$0.32 \pm 0.03$	19.5
2.0 – 3.5	$0.31 \pm 0.02$	20.5
3.5 – 5.0	$0.32 \pm 0.01$	21.0
5.0 – 7.0	$0.31 \pm 0.01$	21.5

TABLE 1

THE DERIVED SLOPES ( $\frac{dN}{dF160W} \propto 10^{\alpha F160W}$ ) OF THE  $F160W$  BAND LUMINOSITY FUNCTIONS FOR R136 TOGETHER WITH THEIR UNCERTAINTIES. THE INNER AND OUTER RADII ARE GIVEN FOR EACH ANNULUS. THE MAXIMUM  $F160W$  BAND MAGNITUDE (50% COMPLETENESS LIMIT) USED TO DERIVE THE FIT IS SHOWN AS WELL.

Xcen	Ycen	$F160W$	$F160W_{error}$
104.546	280.899	19.09	0.04
156.263	148.125	20.28	0.05
121.580	148.709	20.15	0.03
315.194	150.819	20.29	0.03
481.127	152.319	20.27	0.04
69.890	154.680	17.73	0.05
280.115	155.118	19.76	0.01
91.993	157.119	18.87	0.04
443.582	157.392	17.34	0.02

TABLE 2

THE  $F160W$  BAND DETECTED SOURCES IN R 136. THE FULL TABLE IS AVAILABLE ONLINE.

Age(Myr)	Annulus(pc)	Mass range( $M_{\odot}$ )	Slope( $\Gamma$ )	Mass range( $M_{\odot}$ )	Slope( $\Gamma$ )
3	0.6 – 1.0	8.9 – 20	$-1.7 \pm 0.3$	–	–
3	1.0 – 2.0	8.9 – 20	$-1.5 \pm 0.1$	–	–
3	2.0 – 3.0	8.9 – 20	$-1.4 \pm 0.2$	–	–
3	3.0 – 5.0	1.4 – 20	$-1.2 \pm 0.1$	–	–
3	5.0 – 7.0	0.8 – 20	$-0.9 \pm 0.1$	1.4–1.7	$-0.9 \pm 0.2$
2	3.0 – 5.0	1.1 – 20	$-1.0 \pm 0.1$	1.1–1.7	$-1.3 \pm 0.3$
2	5.0 – 7.0	0.7 – 20	$-1.0 \pm 0.1$	0.7–1.7	$-0.8 \pm 0.2$
4	3.0 – 5.0	1.4 – 20	$-1.2 \pm 0.1$	–	–
4	5.0 – 7.0	1.1 – 20	$-1.2 \pm 0.1$	1.1–1.6	$-1.3 \pm 0.4$
2 – 4	3.0 – 5.0	1.4 – 20	$-1.3 \pm 0.1$	–	–
2 – 4	5.0 – 7.0	1.1 – 20	$-1.2 \pm 0.1$	1.1–1.6	$-1.1 \pm 0.4$

TABLE 3

THE DERIVED SLOPES ( $\Gamma$ ,  $dN/d \log M \propto M^{\Gamma}$ ) OF THE MASS FUNCTIONS TOGETHER WITH THE DERIVED UNCERTAINTIES OF THE SLOPES. THE SLOPE OF A SALPETER IMF IN THESE UNITS IS  $-1.35$ . ALL THE FITS WERE PERFORMED OVER THE MASS RANGE INDICATED IN THE TABLE.

Center of mass bin ( $M_{\odot}$ )	0.7	0.9	1.1	1.4	2.0	2.8	3.5	5.0	7.1	8.9	11.2	14.1	17.8	22.4	28.2
Annulus(pc)															
0.6-1.0	0	0	0	0	2	11	13	21	42	51	50	25	18	11	8
1.0-2.0	9	27	44	56	92	155	85	56	111	91	77	48	35	30	10
2.0-3.0	40	74	126	139	163	157	100	53	105	80	55	57	30	17	9
3.0-5.0	283	328	416	380	329	268	137	86	168	111	73	41	40	29	9
5.0-7.0	310	351	355	297	278	202	102	56	108	74	47	43	24	24	6

TABLE 4

THE NUMBER OF STARS PER MASS BIN USED TO DERIVE THE IMF FOR THE 3 MYR ISOCCHRONE. THE NUMBERS HAVE NOT BEEN CORRECTED FOR INCOMPLETENESS.